Computer Methods in Applied Mechanics and Engineering 447 (2025) 118363

Contents lists available at ScienceDirect

Comput. Methods Appl. Mech. Engrg.

journal homepage: www.elsevier.com/locate/cma

A physics-motivated geometric method for overheating prevention in topology optimization for additive manufacturing

Manabendra Nath Das [a], Rajit Ranjan [b], Kai Wu [c], Jun Wu [a], Can Ayas [c,*]

[a] Faculty of Industrial Design Engineering, Sustainable Design Engineering Department, Delft University of Technology, Delft, the Netherlands
[b] Department of Mechanical Engineering, Indian Institute of Technology Jodhpur, Jodhpur, Rajasthan, India
[c] Faculty of Mechanical Engineering, Precision and Microsystems Engineering Department, Delft University of Technology, Delft, the Netherlands

ARTICLE INFO

Keywords:
Topology optimization
Additive manufacturing
Process modeling
Overheating
Thermal modeling

ABSTRACT

Designs generated by topology optimization are often geometrically too complex for conventional manufacturing techniques. While additive manufacturing holds promise for producing such complex designs, several manufacturability constraints must be addressed, including overhang and overheating. Unlike the well-studied overhang constraints, which can be described geometrically, overheating lacks a straightforward and reliable geometric characterization and therefore requires thermal process simulations to identify regions prone to it. However, these simulations are computationally expensive and thus unsuitable for topology optimization, which involves numerous design evaluations. This paper proposes a computationally efficient alternative for detecting zones prone to overheating. The key idea is to estimate local thermal conductivity—and thereby potential overheating—by analyzing the local material distribution. This geometric approach provides a physically motivated approximation of thermal behavior. The method is then integrated into topology optimization, resulting in optimized structures that exhibit clear heat conduction paths to the baseplate. Comparisons with high-fidelity thermal simulations demonstrate the effectiveness and efficiency of the proposed method in mitigating overheating in topology optimization.

1. Introduction

Topology optimization (TO) determines the optimal material distribution within a design domain to achieve a specific objective while meeting a set of constraints. The resulting designs often include complex geometries that are difficult or impossible to produce using conventional manufacturing methods, but can be fabricated using additive manufacturing (AM). However, AM introduces its own process-specific limitations that must be considered during the design stage. These constraints should be integrated into the topology optimization process to ensure manufacturability. Previous research has addressed several of these limitations, including overhang control (e.g., van de Ven et al. [1], Zhang et al. [2], Garaigordobil et al. [3], Langelaar [4], Wu et al. [5], Gaynor et al. [6]), distortion reduction (e.g., Misiun et al. [7], Miki and Yamada [8], Wildman and Gaynor [9]), and residual stress management (e.g., Xu et al. [10], Cheng et al. [11], Allaire and Jakabčin [12]). One important but less extensively studied constraint is local overheating, or heat accumulation, which can occur during metal AM and lead to print failure, surface roughness, defects, and degraded material quality.

In metal AM, material addition is achieved by selectively melting and fusing the powder through a high-energy beam in the case of powder bed fusion (PBF), or by deposition of molten material on the previously deposited solid part in directed energy deposition

* Corresponding author.
E-mail address: c.ayas@tudelft.nl (C. Ayas).

https://doi.org/10.1016/j.cma.2025.118363
Received 23 June 2025; Received in revised form 22 August 2025; Accepted 1 September 2025
Available online 20 September 2025

(DED). Each new layer introduces heat in both cases, causing the underlying material to experience repeated heating and cooling cycles. Heating and subsequent cooling are associated with the heat flow from the newly deposited, topmost layer, through the previously deposited layers, ultimately into the baseplate, which acts as a heat sink. Severe heat accumulation occurs when the flow of heat to the baseplate is obstructed [13,14]. This leads to local overheating and a multitude of problems, such as an enlarged melt pool [15], higher residual stresses [16], and even build failure [17,18]. Poor surface quality due to dross formation and balling is also directly associated with overheating [19]. Finally, heat accumulation can adversely influence the microstructure, which dictates the material properties [20–22]. Thus, it is of paramount importance to mitigate local overheating.

The factors contributing to local overheating can be broadly classified into three categories. The first category pertains to AM process parameters such as printing speed, fabrication sequence, and power. Since these parameters influence the heat input, they significantly affect the part's local thermal history [23]. The second category involves the thermal properties of the material. For instance, materials with high thermal diffusivity enable faster heat dissipation. Lastly, the third category relates to part design. For instance, geometric features that hinder efficient heat evacuation lead to local overheating [19]. In this paper, we focus on heat accumulation due to the part design while assuming other factors to be constant.

Overhanging geometric features are known to contribute to heat accumulation, as overhanging layers lack sufficient solid material beneath them to facilitate effective heat dissipation. This is because the conductivity of air (in DED) or loose powder (in PBF) is much less than that of the solid metal [24,25]. This obstruction in heat flow causes local overheating [13,19]. Geometrical design guidelines have been proposed to limit the overhang angle (the angle between the part surface and the baseplate), to be greater than a critical value θ_{cr} ranging between 40°–50° [26–28]. Many methods have been developed to avoid overhangs in TO, e.g., Liu et al. [29], and Langelaar [30]. However, Adam and Zimmer [31] experimentally demonstrated the persistence of thermal bottlenecks, even when overhangs satisfy the critical value, particularly funnel-shaped structures narrowing down along the heat conduction path. Moreover, Ranjan et al. [32] found that overhangs with identical overhang angles exhibit different thermal behavior depending on the heat evacuation capacity of the local geometric layout. This also implies that explicit overhang control can become too restrictive. Additionally, geometric features other than overhangs are also susceptible to overheating. Thin features that have limited solid material in their vicinity can obstruct the heat flow and exhibit overheating [15,33]. Therefore, it is necessary to identify and avoid geometric features causing overheating.

As discussed above, a purely geometric constraint on the overhang angle is not sufficient to prevent overheating, and at the same time, can be too restrictive. The latter happens when the features in the vicinity of an acute overhang may facilitate heat conduction to the baseplate, which can render an overhanging feature permissible in the design. Consequently, a TO scheme that could prevent overheating by explicitly accounting for the thermal evolution of the AM process would have significant advantages over the geometric design rules. Various methods have been developed in the literature that accurately determine the thermal history of the part during the AM process [34–36]. The models are, however, computationally expensive due to the multi-physics and multi-scale nature of the AM process [37]. Hence, a significant research effort exists to develop simplified AM models that capture thermal evolution during AM. Provided they are computationally efficient, these methods can be incorporated into topology optimization. A detailed discussion of relevant literature is provided below.

Zhou et al. [38] successfully integrated a transient thermal AM simulation with density-based TO to design support structures with efficient thermal conductive capabilities for the laser powder bed fusion (LPBF) process. Similarly, Miki and Yamada [8] proposed a TO approach that incorporates thermally induced distortion within the optimization process. Mishra et al. [20] utilized TO to control solid-state phase fractions based on the thermal history, thereby influencing the resulting mechanical properties. Although these transient thermal simulations are accurate, they are computationally expensive and can render the optimization process intractable for large-scale problems, especially in three dimensions. The studies by Ranjan et al. [39] and Ranjan et al. [40] are particularly relevant to this work, as they incorporate a simplified, approximate thermal model to prevent overheating in density-based TO. This AM process model [32] relies on a series of steady-state thermal analyses within parts of the domain to detect zones prone to local overheating. To the best of the authors' knowledge, this method is among the most computationally efficient available in the literature, and is grounded in physical principles of heat conduction. Its computational efficiency and accuracy have been numerically demonstrated by Ranjan et al. [39,40], and the mitigation of overheating has been validated experimentally by Ranjan et al. [40]. However, the approach of Ranjan et al. [39,40] still requires performing multiple steady-state thermal analyses within smaller sub-domains at each TO iteration. While significantly faster than fully transient thermal models, this process remains computationally intensive when applied to large-scale, real-world problems with millions of degrees of freedom or more. Therefore, there remains a need to increase the computational efficiency of AM process simulation further so that it can reliably prevent overheating in large, three-dimensional TO problems.

This paper introduces a novel physics-motivated geometrical method for detecting overheating zones in additively manufactured parts. A conductivity map is constructed based on the local solid material distribution around all material points. The local conductivity propensity at each material point is then used to compute a pseudo-temperature field that reveals whether it is susceptible to local overheating during manufacturing. In contrast to transient or even simplified thermal simulations, the proposed approach offers negligible computational cost. This pseudo-temperature is then used to formulate a constraint in TO to prevent overheating.

The paper contents are structured as follows: the formulation of the proposed geometric overheating detection method, its application, and effectiveness in detecting local overheating are demonstrated in Section 2.1. The geometric overheating detection method as a constraint and its integration with TO is established in Section 2.2. The numerical examples of optimized designs are discussed in Section 3. A comparative study of the designs obtained using the proposed overheating constraint and other geometric approaches from the literature to eradicate overhangs is presented in Section 3.1. The TO scheme's extension to 3D is demonstrated in Section 3.2.

The computational cost of different approaches in both 2D and 3D is compared in Section 3.3. The conclusions and future scope of the work are given in Section 4.

2. Methodology

This section presents the physics-motivated geometric overheating detection method and its integration as a constraint in TO. First, physics-motivated geometric overheating detection is described. The method's effectiveness in detecting overheating is validated by a high-fidelity AM process model. Subsequently, the overheating detection method is used as a constraint and incorporated into the TO.

2.1. Geometric overheating detection

During the AM process, the moving heat source raises the local temperature of the material point directly under the heat source and surroundings, including several preceding layers, referred to as the heat-affected zone. The temperature field in the heat-affected zone exhibits a gradient, with higher temperatures near the heat source gradually diminishing with the distance from the source, as modeled in Mirkoohi et al. [41]. Ranjan et al. [32] utilized an analytical solution of the 1D transient heat equation to show that the maximum temperature of a newly added material point is unaffected by increasing the domain size beyond a critical thermal interaction length defined as

$$\kappa = \sqrt{\alpha t_h}, \tag{1}$$

where α is the thermal diffusivity of the material given as

$$\alpha = \frac{k}{\rho C_p}, \tag{2}$$

where k, ρ, and C_p are the thermal conductivity, density, and specific heat of the material, respectively. The heating time t_h depends on the AM process parameters. For the LPBF process, it is estimated as

$$t_h = \frac{A}{hv}, \tag{3}$$

where A is the area of the layer, h is the hatch spacing and v is the laser scan velocity [32]. For further details, readers are referred to [42]. This observation implies that the peak temperature near the heat source primarily depends on the heat transfer within a finite heat conduction domain. In 3D, assuming isotropic conduction, this domain becomes a hemisphere with a radius κ. Fig. 1 shows the semicircular 2D representation of the heat conduction domain. If a heated material point has abundant solid material within its heat conduction domain, ample heat conduction prevents overheating and vice versa. Moreover, within the conduction domain, material points closer to the heat source, and those positioned symmetrically opposite the build direction, have a greater influence on heat evacuation to prevent overheating.

To determine the heat evacuation capacity of each material point, it remains to calculate the total volume of the solid weighted according to the source proximity and orientation based on build direction **b** in the conduction domain. We call this *Conductivity Estimation*, and the heat conduction domain in the remainder is referred to as the conductivity domain. Note that conductivity here refers to the local heat evacuation capability towards the baseplate, not the thermal material property. Yeung et al. [43] introduced a similar approach for in-situ laser power regulation utilizing the proportion of solid and powder material surrounding the melt pool. Although related, the study did not utilize the idea in the context of part design, which is the purview of this paper.

Consider the part shown in Fig. 1 in a discretized domain of finite elements, analogous to the density-based TO design domain. The build direction is along the y axis indicated by **b**. A discrete pseudo-density field is assumed on each element, where $\rho = 1$ (blue) indicates solid and $\rho = 0$ (white) indicates loose powder or air for PBF and DED, respectively. Consider the instance element i, which is under the influence of the heat source. The set of elements in the conductivity domain of element i is given as S_i. If the element center coordinates of elements i and j are (x_i, y_i) and (x_j, y_j), respectively, and κ is the conductivity domain radius.

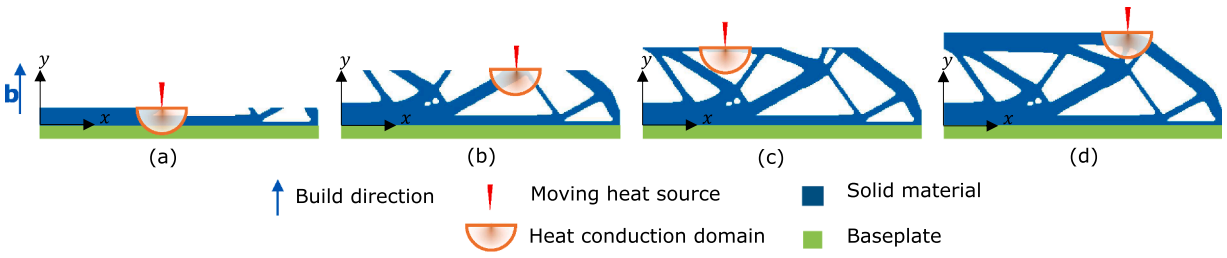

Fig. 1. Schematic illustration of the heat conduction domain on a part during various stages (a–d) of AM. The part is built over a baseplate, and the build direction is indicated by **b**. The layer-by-layer deposition of the material through the moving heat source and the heat conduction domain is shown.

The element $j \in S_i$ if $\sqrt{(x_i - x_j)^2 + (y_i - y_j)^2} \leq \kappa$ granted $y_j \leq y_i$ for the given build direction. The latter condition ensures that only the previously deposited layers are considered within the conductivity domain. We introduce weight functions to incorporate the influence of elements $j \in S_i$ on the heat evacuation capacity of element i. These weights penalize the contribution of elements $j \in S_i$ in the radial and angular directions, such that a higher contribution of conduction is assumed for elements in closer proximity and along the build orientation of the element i. Thus the radial weight function $\tilde{w}$ and angular weight function $\hat{w}$ of element $j \in S_i$ are given as:

$$ {}^{i}\tilde{w}_j = \frac{\kappa - \sqrt{(x_i - x_j)^2 + (y_i - y_j)^2}}{\kappa}, \tag{4} $$

$$ {}^{i}\hat{w}_j = \frac{\tan^{-1}\left(\frac{y_i - y_j}{x_i - x_j}\right)}{\pi/2}, \tag{5} $$

normalized between 0 and 1. The prescript indicates that the weight function for the element i. The final weight function ${}^{i}w_j = {}^{i}\tilde{w}_j \, {}^{i}\hat{w}_j$.

Fig. 2c indicates how the elements in the conductivity domain given by Fig. 2d will be weighted with radial and angular weight functions, as shown in Fig. 2a and b, respectively. The conductivity estimation is performed for every solid element by calculating

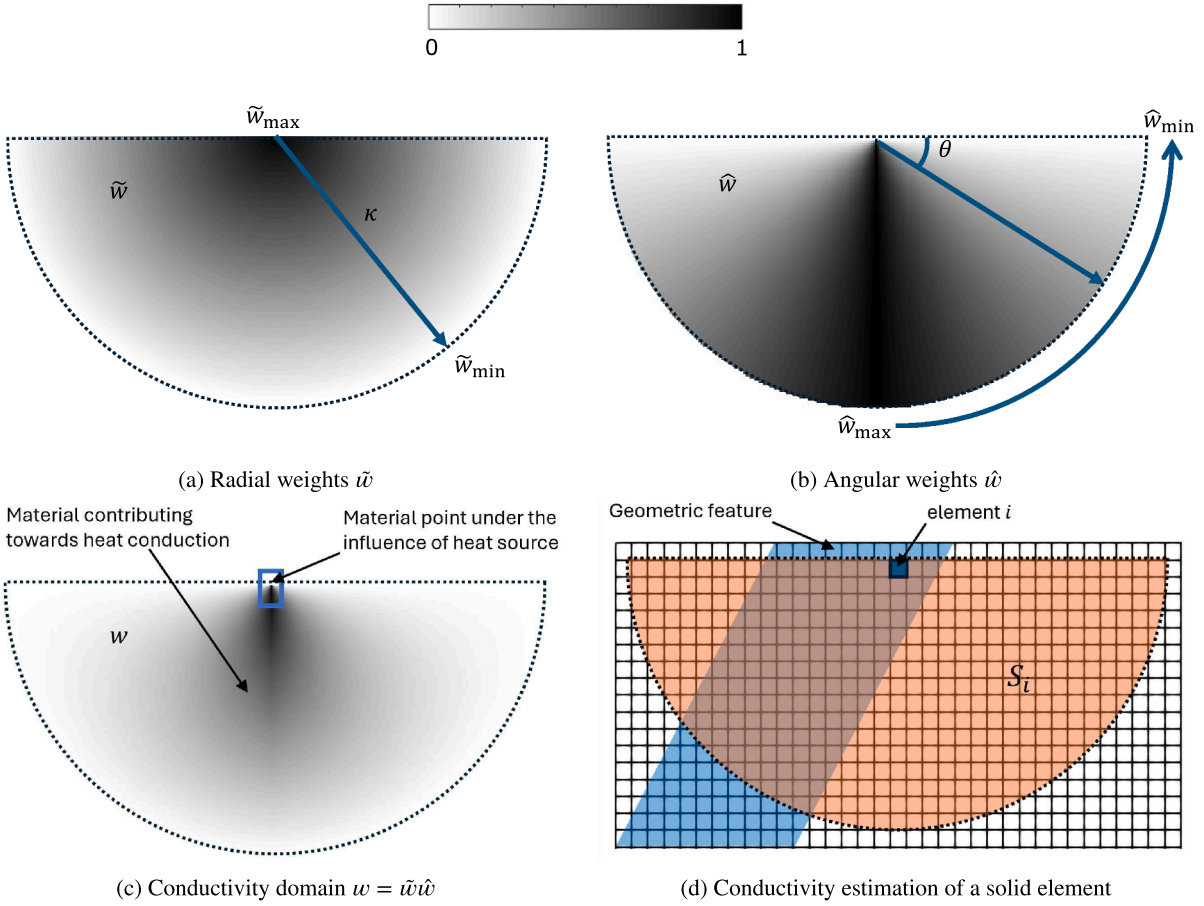

(a) Radial weights $\tilde{w}$

(b) Angular weights $\hat{w}$

(c) Conductivity domain $w = \tilde{w}\hat{w}$

(d) Conductivity estimation of a solid element

Fig. 2. Illustration of the weight functions used to represent the physics of heat conduction geometrically. The material points with a higher influence on heat conduction are shown in a darker shade, as shown by the color bar. The radial weights $\tilde{w}$ (a) penalize the material inside the heat conduction domain of radius κ following the distance to the material under the influence of the heat source, $\tilde{w}_{max} = 1, \tilde{w}_{min} = 0$ being the maximum and minimum value of the radial weights, respectively. The angular weights $\hat{w}$ (b) penalize the material concerning the misalignment with the build direction measured with angle θ from the horizontal with $\hat{w}_{max} = 1, \hat{w}_{min} = 0$ being the maximum and minimum value of the angular weights, respectively. The final weight function w is shown in (c). The conductivity domain (d) on a part discretized with a structured mesh where the local conductivity of the central element i of a geometric feature is evaluated using the weighted densities of the elements $j \in S_i$. (For interpretation of the references to color in this figure legend, the reader is referred to the web version of this article.)

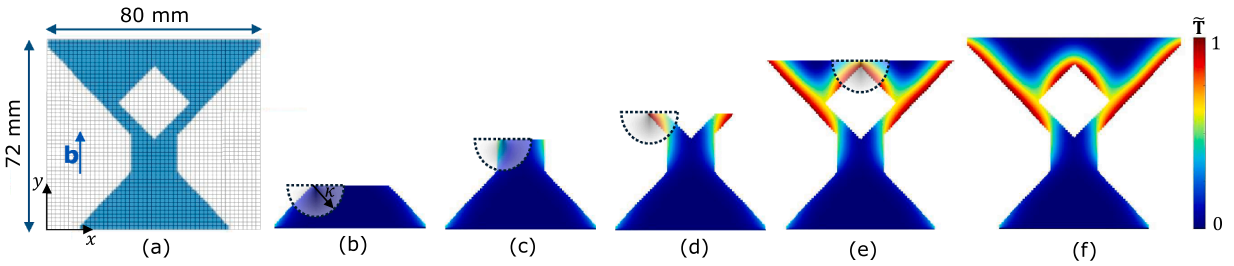

Fig. 3. Illustration of the conductivity estimation and detecting heat accumulation zones for a funnel-shaped part. The build direction is given by **b**. The discretized part geometry on a structured mesh is shown in (a). The snapshots of the hotspot map during various stages of AM are shown in (b–e). The final hotspot map of the part is shown in (f).

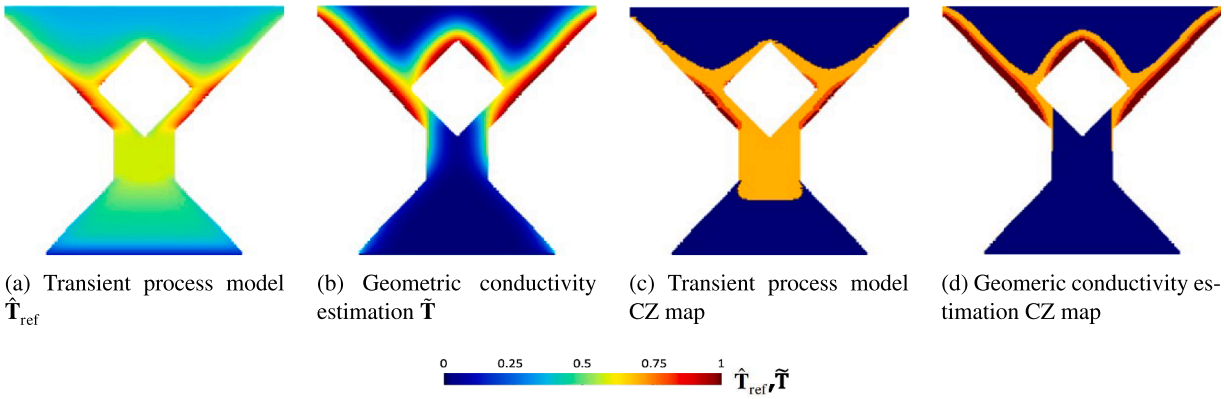

Fig. 4. The hotspot maps for (a) high fidelity transient thermal process model and (b) conductivity estimation analysis. The corresponding critical zone (CZ) maps showing contour levels of only 0.5 and above of the maximum temperature of the hotspot map are presented in (c) and (d), respectively.

local conductivity for element i as:

$$\mu_i = \frac{\sum_{j \in S_i}^{n} \rho_j{}^i w_j}{\sum_{j \in S_i}^{n} {}^i w_j}, \tag{6}$$

which is constrained within the range [0, 1]. A higher value of μ indicates that the element i has an abundant material in its conductivity domain distributed favorably, suggesting good heat conduction and vice versa. This metric resembles the one applied in the local volume constraint for generating porous structures in Wu et al. [44]. However, the local volume constraint does not account for the direction of material deposition in AM. To get a qualitative indication of the temperature in the part, we define a pseudo-temperature $\tilde{T}_i$ for element i as:

$$\tilde{T}_i = 1 - \mu_i. \tag{7}$$

A higher pseudo-temperature implies susceptibility to local overheating. Note that the pseudo-temperature values only qualitatively indicate the overheating tendency of design features and do not represent physical temperatures. The pseudo-temperature field array $\tilde{\mathbf{T}}$ of the entire domain will be referred to as the hotspot map.

The conductivity estimation is exemplified using the discretized 2D geometry shown in Fig. 3a. The part geometry encapsulates features that are responsible for local overheating, such as overhangs, thin sections, and funnel-like features [19,22,28,39]. The dimension of the part is 80 mm × 72 mm. All overhangs have an overhang angle of $\theta = \pm 45°$. The conductivity domain radius, κ = 12 mm, is determined based on the thermal interaction length corresponding to the process parameters used in Ranjan et al. [32] and the material properties of Ti-6Al-4V at its melting point, as reported in Chiumenti et al. [45]. For other commonly used materials in LPBF, such as AISI 316L, Cr-Co, and Al-Si alloys, κ becomes approximately 10 mm, 9 mm, and 26 mm, respectively, assuming identical process parameters and material properties at the melting point [46–48].

The conductivity estimation for the entire part is performed simultaneously for all layers, as the layer-by-layer printing sequence is taken into account by the orientation and shape of the conductivity domain. The hotspot map of the temperature field $\tilde{\mathbf{T}}$ is generated using Eq. (7) and is shown in Fig. 3f. Fig. 3b–e shows the hotspot maps of the intermediate stages of the AM process. As can be seen in Fig. 3b,c, since there are a large number of solid elements that contribute to heat conduction, the heat evacuation is adequate, and overheating risks are low, as observed from the hotspot maps. The overhanging feature in Fig. 3d increases the pseudo-temperature, since the number of solid elements within the respective conductivity domains diminishes. A comparable reduction in local conductivity is observed at the overhang junction, as illustrated in Fig. 3e. Note that although all overhangs share the same

inclination angle (45°), the resulting pseudo-temperature fields slightly differ due to variations in the surrounding geometry. These findings are in agreement with the experiments performed in Adam and Zimmer [31], Van Toor [49] and Patel et al. [50].

Next, the conductivity estimation method is compared with an LPBF transient thermal simulation chosen as a reference. The reference thermal LPBF process model follows [32]. Heat loss through conduction, convection, radiation, and the temperature-dependent thermal properties of Ti-6Al-4V from Chiumenti et al. [45] is accounted for. The part-powder/air interface is considered adiabatic. The element birth-and-death method is used to mimic the growing domain during AM [51,52]. A lumped layer analysis is incorporated that combines 10 AM layers into one super layer. The element size is 0.5 mm, corresponding to a layer thickness of 50 μm. In each simulation cycle, where a new set of elements is introduced, the deposited super layer undergoes heating with a uniform volumetric heat flux for t_h. This is followed by a cooling time during which the heat flux is turned off. We select an estimated cooling time of 50 s, which is ten times the typical recoater time of 5 s, to take into consideration the layer lumping [52,53]. This choice ensures a conservative estimation of heat accumulation between successive layers. The bottom surface of the baseplate acts as a heat sink at a constant temperature of 180 °C. For more details about the transient simulation, readers are referred to Ranjan et al. [32].

For a consistent comparison, the maximum temperature field $\mathbf{T}$ from the high-fidelity simulation is normalized by its maximum value, $\hat{\mathbf{T}}_{\text{ref}} = \mathbf{T}/\max(\mathbf{T})$, to obtain the hotspot map shown in Fig. 4a. The hotspot map of conductivity estimation in Fig. 4b is similar, though not identical, to that of the high-fidelity simulation, since the former represents a simplified geometric approximation of heat conduction. The conductivity estimation does not provide accurate predictions in regions with abundant material, such as the central portion of the design. However, the high-fidelity simulation in Fig. 4a reveals that these regions remain at relatively lower temperatures and are therefore not prone to overheating. Since our primary objective is to identify areas that are critical with respect to overheating, the conductivity estimation is designed to emphasize regions with less material, which are more susceptible to thermal accumulation. To this end, we introduce a critical zone (CZ) map, obtained by showing contour levels of only 0.5 and above of the hotspot map. Fig. 4c and d compare the CZ maps extracted from the high-fidelity thermal simulation and the conductivity estimation. The CZ maps show excellent agreement around overhanging and thin geometric features, while the conductivity estimation is up to 1400 times computationally cheaper than the high-fidelity transient thermal simulation. Thus, the geometric conductivity estimation method is both accurate and computationally efficient for overheating detection.

It is important to note that the conductivity estimation may underestimate overheating in cases where long overhanging gaps smaller than the conductivity domain are present. In such situations, the conductivity estimation can yield an artificially high local conductivity value due to the presence of solid material within the conductivity domain, even though the solid region above the gap itself may be prone to overheating. The radial and angular weight functions given by Eqs. (4) and (5) alleviate this issue to some extent, but this limitation is still evident in the formulation of the overheating constraint (see Fig. 6b). Nevertheless, the issue primarily affects overheating detection in static geometries and is resolved when the method is integrated with robust topology optimization, as discussed in Section 2.2.

2.2. Integration with TO

The primary goal of this paper is to develop a novel TO method to prevent local overheating during the AM process. Therefore, we consider a linear elastic compliance minimization objective and a global volume constraint. The design domain is discretized with a structured mesh of bi-linear, four-noded elements. A commonly used load case of the half MBB beam is used for optimization. Fig. 5 shows the design domain dimensions, the point load, and the boundary conditions for the half MBB beam. The design domain is discretized into 180×60 elements, with an element size of 1 mm × 1 mm.

The compliance minimization TO is given as follows:

$$\min_{\rho} : \quad c(\boldsymbol{\rho}) = \mathbf{U}^{\mathrm{T}}\mathbf{K}\mathbf{U} = \sum_{i=1}^{N} E_i(\tilde{\rho}_i)\mathbf{u}_i^{\mathrm{T}}\mathbf{k}_0\mathbf{u}_i, \tag{8a}$$

$$\text{subject to:} \quad \mathbf{K}\mathbf{U} = \mathbf{f}, \tag{8b}$$

$$f(\boldsymbol{\rho}) = V(\boldsymbol{\rho})/V \leq v_f, \tag{8c}$$

$$\mathbf{0} \leq \boldsymbol{\rho} \leq \mathbf{1}. \tag{8d}$$

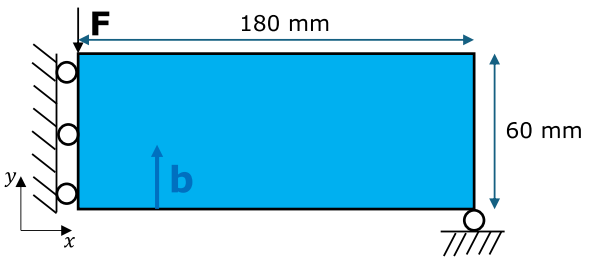

Fig. 5. Half MBB beam problem used for the optimization. The load **F**, boundary conditions with roller support on the left edge and the bottom right corner, dimensions of the design domain, and build direction **b** are as shown.

Here c is the compliance of the structure, and $\boldsymbol{\rho}$ is the array of pseudo-densities which are design variables. The subscript i denotes the element number, and N is the total number of elements. $\mathbf{U}$ is the global nodal displacement array, $\mathbf{u}_i$ is the element displacement vector, $\mathbf{f}$ is the global nodal force array, $\mathbf{K}$ is the global stiffness matrix and is assembled from element stiffness matrices $\mathbf{k}_i = E_i(\tilde{\rho}_i)\mathbf{k}_0$, where $\mathbf{k}_0$ is the element stiffness matrix for an element with unit Young's Modulus. Here, $\tilde{\rho}_i$ is the filtered density given by Bruns and Tortorelli [54] to impose a length scale control and avoid checkerboarding, and $E_i(\tilde{\rho}_i)$ is Young's modulus corresponding to the element i, interpolated via the solid isotropic material with penalization (SIMP) [55], given by:

$$E_i(\tilde{\rho}_i) = E_{\min} + \tilde{\rho}_i^p(E_0 - E_{\min}), \tag{9}$$

where $E_0 = 1$ is the Young's modulus of a solid element. A small value of $E_{\min} = 10^{-9}$ is assigned to prevent the singularity of the global stiffness matrix, and $p = 3$ is the penalization factor. The global volume constraint is $f(\boldsymbol{\rho})$, the material volume is $V(\boldsymbol{\rho}) = \sum_i \tilde{\rho}_i v_0$, where v_0 is the constant area or volume of the element in 2D and 3D, respectively. The design domain volume is V, and v_f is the prescribed maximum volume fraction.

It remains to incorporate an overheating constraint into the TO using the conductivity estimation method. To prevent overheating, the maximum pseudo-temperature across the domain is constrained to remain below a critical temperature value, T_{cr}. As a result, the optimized design is expected to have a geometric layout that will allow for efficient heat evacuation towards the baseplate and thus reduce the risk of local overheating. Note that T_{cr} is a tunable parameter between 0 and 1, and a smaller value leads to a stricter constraint. The conductivity domain radius $\kappa = 12\,\text{mm}$ is calculated from the process parameters and material properties mentioned earlier.

The local conductivity derived in Eq. (6) is modified by penalizing the densities of elements in the conductivity domain by the conductivity penalization factor q, identical to a SIMP penalization p. Thus, the penalized local conductivity $\bar{\mu} \in [0,1]$ for an element i is calculated as:

$$\bar{\mu}_i = \frac{\sum_{j\in S_i}^{n} \tilde{\rho}_j^{q_i} w_j}{\sum_{j\in S_i}^{n} {}^{i} w_j}. \tag{10}$$

This is done to prevent the constraint from being artificially satisfied by intermediate densities during the initial optimization iterations and to promote better convergence. Consequently, the hotspot map showing a pseudo-temperature $\bar{T} \in [0,1]$ for each element i can be calculated as:

$$\bar{T}_i = (1 - \bar{\mu}_i). \tag{11}$$

To improve the computational efficiency, the maximum value of the hotspot map $\bar{\mathbf{T}}$ is used for the constraint as:

$$\max(\bar{\mathbf{T}}) \leq T_{\text{cr}}. \tag{12}$$

The maximum operator is non-differentiable, making it unsuitable for calculating the sensitivities required in gradient-based optimization. A P-mean aggregation scheme specifies the constraint, a smooth, continuous function used to find the maximum temperature over the entire design domain. Thus, the overheating constraint is formulated as:

$$\left[\frac{1}{N}\sum_{i}^{N}(\bar{T}_i)^P\right]^{1/P} \leq T_{\text{cr}}. \tag{13}$$

Here, $\bar{T}_i$ is the ith member of the array $\bar{\mathbf{T}}$, P is the P-mean exponent. P-mean tends to underestimate the maximum temperature. This error can be reduced by increasing the P value. However, as $P \to \infty$, the P-mean asymptotes to the real maximum value, thus becomes non-smooth, resulting in inaccurate estimation of the true maximum, which leads to overconservative designs. Therefore, the maximum predicted by the P-mean is corrected by scaling it with the true maximum $\max(\bar{\mathbf{T}})$ according to an adaptive scheme proposed by Le et al. [56]. Thus, from Eqs. (11) and (13), the overheating constraint after including a scaling factor α becomes:

$$g = \alpha\left[\frac{1}{N}\sum_{i}^{N}(1 - \bar{\mu}_i)^P\right]^{1/P} \leq T_{\text{cr}}, \tag{14}$$

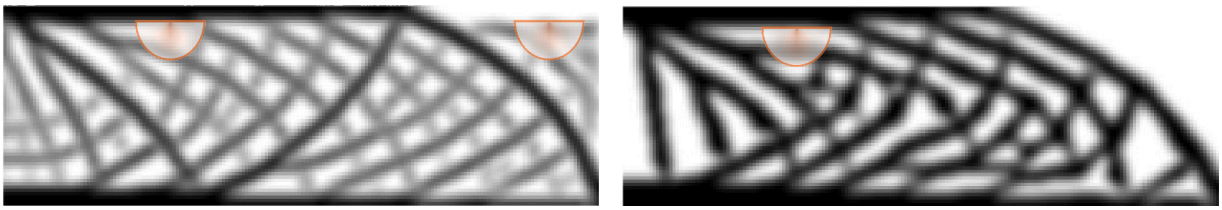

(a) Overheating constraint Eq. (14) for $T_{\text{cr}} = 0.8$ (b) Overheating constraint Eq. (16) for $T_{\text{cr}} = 0.8$

Fig. 6. TO (a) without the relaxation factor ϵ, (b) with the relaxation factor ϵ in the overheating constraint. The orange semicircle represents the conductivity domain.

where α is defined as the ratio between the true maximum temperature obtained from the design domain and the P-mean of the previous iteration, given by:

$$\alpha_{(I)} = \left(\frac{\max(\bar{\mathbf{T}})}{\left[\frac{1}{N} \sum_i^N (1-\bar{\mu}_i)^P \right]^{1/P}} \right)_{(I-1)}, \tag{15}$$

where I is the current iteration number. Note that, since α changes discontinuously, the adaptive scheme may cause convergence issues. Therefore, it is updated every 25 iterations with a continuation scheme, solving this non-convergence issue. The value of P is set to be 25, which has good accuracy and convergence over the design iterations.

Applying the overheating constraint given in Eq. (14) on a standard TO design from Eq. (8) creates impractical designs with isolated geometries outside the base design, as shown in Fig. 6a. The optimizer is compelled to satisfy the minimum local conductivity of the elements everywhere in the design domain, even for the void elements $\tilde{\rho}_i \approx 0$ that have a large number of void elements in their conductivity domain ($\tilde{\rho}_j \approx 0 \; \forall \; j \in S_i$). To relax the constraint in the void elements that are outside the base design, the pseudo-temperature $\bar{\mathbf{T}}$ is multiplied by a relaxation factor $\boldsymbol{\epsilon}$. The relaxation factor for an element i is $\epsilon_i = \tilde{\rho}_i^r$, where $\tilde{\rho}_i$ is the filtered density of the element and r is the relaxation exponent. The ϵ controls the $\bar{\mu}$ value required to satisfy the overheating constraint for an element i. In the void phase, the relaxation factor ensures that the constraint is satisfied by having a very low requirement of $\bar{\mu}$. The value of $r = 0.05$ is chosen as it had the best convergence among other values of r for our choice of $T_{\text{cr}} = 0.8$. A comprehensive study of how r varies with q and T_{cr} is provided in Appendices A.1 and A.2, respectively. The overheating constraint then becomes:

$$g = \alpha \left[\frac{1}{N} \sum_i^N ((1-\bar{\mu}_i)\tilde{\rho}_i^r)^P \right]^{1/P} \leq T_{\text{cr}}, \tag{16}$$

where α for an iteration I is now given as:

$$\alpha_{(I)} = \left(\frac{\max(\bar{\mathbf{T}}\boldsymbol{\epsilon})}{\left[\frac{1}{N} \sum_i^N ((1-\bar{\mu}_i)\tilde{\rho}_i^r)^P \right]^{1/P}} \right)_{(I-1)}. \tag{17}$$

Although the modified overheating constraint suppresses the emergence of isolated geometries in the void regions, another problem persists in the topology-optimized designs, as illustrated in Fig. 6b. Even after penalizing elements in the conductivity domain using the weight function defined in Eqs. (4) and (5), the design minimizes the compliance through closely spaced design features in the majority of the design domain. As long as the void phase between the neighboring features is considerably smaller than the radius of the conductivity domain, the overheating constraint can be artificially satisfied, despite the heat conduction pathway being disconnected due to the void phase separating solid phases. Consequently, this design will still be prone to overheating if assessed by the transient thermal model introduced earlier, and therefore, it should be avoided. Moreover, the design exhibits a non-discrete character due to the smoothing effect of the density filter at the boundaries between solid and void phases, which can be avoided by using a Heaviside projection.

To solve the issue of the emergence of small gaps disconnecting solid phases, the overheating constraint is incorporated in the robust TO given by Wang et al. [57]. The formulation provides length-scale control on both the solid and void phases. It uses three designs called the eroded, intermediate, and dilated designs, with the projected densities $\bar{\tilde{\rho}}^e$, $\bar{\tilde{\rho}}^i$, and $\bar{\tilde{\rho}}^d$, respectively. Based on the projection thresholds, filtered design variables are projected to 1 if they are greater than the threshold or zero if they are lower than the threshold through:

$$\bar{\tilde{\rho}} = \frac{\tanh(\beta\eta) + \tanh(\beta(\tilde{\rho} - \eta))}{\tanh(\beta\eta) + \tanh(\beta(1-\eta))}, \tag{18}$$

where β determines the sharpness of the projection, η and $\bar{\tilde{\rho}}$ are the projection threshold and projected design variable, respectively. The solid features smaller than the density filtering domain are projected to the void phase in the eroded design. The overheating constraint is applied to this eroded design. It ensures that sufficient solid facilitates the heat conduction within every solid element's conductivity domain, such that the pseudo-temperature remains below T_{cr}. Subsequently, voids smaller than the density filtering domain are projected to the solid phase in the dilated design. As a result, small gaps are eliminated from the final intermediate design, yielding a more robust design and reducing the risk of local overheating.

Lazarov et al. [58] demonstrated that using only the eroded design is sufficient for conservative compliance minimization, as it exhibits the highest compliance among the three designs. The robust TO problem with the overheating constraint is defined as:

$$\min_{\rho} : \quad c(\boldsymbol{\rho}) = \mathbf{U}^{e\mathrm{T}} \mathbf{K}(\bar{\tilde{\rho}}^e)\mathbf{U}^e = \sum_{i=1}^N E_i(\bar{\tilde{\rho}}_i^e)\mathbf{u}_i^{e\mathrm{T}} \mathbf{k}_0 \mathbf{u}_i^e, \tag{19a}$$

$$\text{subject to} \quad \mathbf{K}(\bar{\tilde{\rho}}^e)\mathbf{U}^e = \mathbf{f}, \tag{19b}$$

$$f(\boldsymbol{\rho}) = \frac{V_d}{V} \leq V_d^*, \tag{19c}$$

$$g(\boldsymbol{\rho}) = \alpha \left[\frac{1}{N} \sum_i^N \left((1-\bar{\mu}_i^e)(\bar{\tilde{\rho}}_i^e)^r \right)^P \right]^{1/P} \leq T_{\text{cr}}, \tag{19d}$$

$$\mathbf{0} \leq \boldsymbol{\rho} \leq \mathbf{1}. \tag{19e}$$

Here c, $\mathbf{U}^e$, $\mathbf{K}$, $\mathbf{u}_i^e$ are the compliance, global displacement array, global stiffness matrix, and element displacement array, respectively, of the eroded structure. The volume constraint is imposed on the dilated design as it has the highest volume among the three designs. Every 20 iterations the volume fraction of the dilated design is updated as $V_d^* = \frac{v_f}{V_i} V_d$, where $V_d = \sum_i \bar{\rho}_i^d v_0$ is the volume of the dilated design, so that the volume of the intermediate design V_i remains equal to a prescribed value v_f. The overheating constraint is given by $g(\boldsymbol{\rho})$, and $\bar{\mu}_i^e$ is the penalized local conductivity of the eroded densities. The sensitivity analysis of the overheating constraint is given in Appendix A.4.

3. Results

The parameters used for the TO and conductivity estimation are given in Table 1. The optimization algorithm used is the method of moving asymptotes (MMA) by Svanberg [59], with default parameters. The projection sharpness β is set to 1 and incrementally increased every 100 iterations to a maximum of 16. This is done to have a smoother transition from the intermediate design and give the constraint enough time to modify the design variables, leading to better convergence. The density filter radius is $R = 4$ mm, corresponding to one-third of the conductivity domain radius κ. Using a smaller value could potentially lead to gaps between solid regions. The implications of the choice of κ and R are discussed in Appendix A.3. The result of the robust TO problem from Eq. (19) and the progression of the design during the optimization can be seen in Fig. 7. This also illustrates how much P-mean underestimates the maximum temperature in the design domain and scaling to the true maximum is required, as explained in Section 2.2. The scaled P-mean maximum at the end of the iteration loop, denoted by $\bar{T}^e_{\max}$, where superscript e stands for the eroded design, serves as an indicator of whether the overheating constraint is satisfied. The convergence criterion is determined by the number of iterations required for $\bar{T}^e_{\max}$ to reach T_{cr}; a lower T_{cr} typically demands more iterations for convergence.

Table 1
Robust TO parameters for the conductivity estimation design.

Parameters	Values
SIMP penalization	3
Volume fraction v_f	0.5
Poisson's ratio	0.3
Density filter radius R (mm)	4
Critical temperature T_{cr}	0.8
Conductivity penalization factor q	3
Relaxation exponent r	0.05
Conductivity domain radius κ (mm)	12
Projection sharpness $\beta_{\max}$	16
Threshold eroded η_d	0.75
Threshold intermediate η_i	0.5
Threshold dilated η_d	0.25
P-mean exponent P	25
No.of iterations	600
Move limits	0.2
Constraint scaling parameter (MMA) c_0	2500

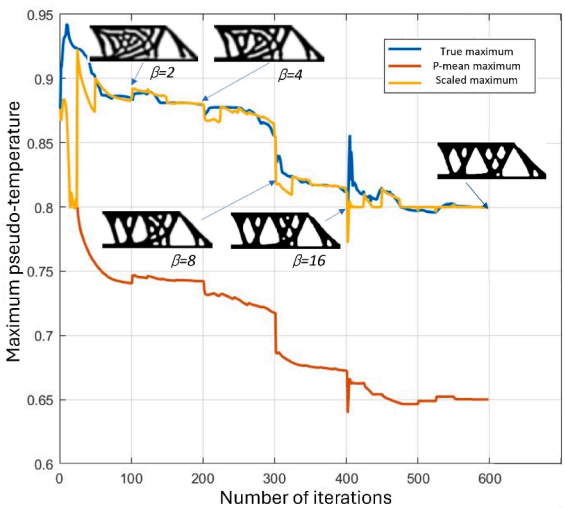

Fig. 7. The scaled P-mean maximum over the TO iterations showing the overheating constraint being satisfied.

The comparison between the robust TO designs with and without the overheating constraint is shown in Fig. 8. The hotspot maps are generated post-optimization using Eq. (11) on the intermediate designs, and the maximum pseudo-temperature in the map is denoted by $\bar{T}_{\max}$. Note that the eroded design has the lowest volume out of intermediate and dilated designs, and thus, $\bar{T}_{\max}$ computed on the intermediate design is lower than $\bar{T}^{e}_{\max}$, ensuring safer final designs. In Fig. 8b, the reference design without overheating constraint indicates a high risk of local overheating near the overhangs with a maximum pseudo temperature value of $\bar{T}_{\max} = 0.97$. Preventing such overheating requires sufficient material distribution within the conductivity domain of each solid element. The overheating constraint facilitates this redistribution, promoting conductive pathways for effective heat evacuation toward the base plate, as illustrated in Fig. 8c. Moreover, the teardrop-shaped voids prevent thermal bottlenecks in the design. Consequently, the maximum pseudo-temperature is just $\bar{T}_{\max} = 0.78$. The structure's compliance is only 23 % higher than the reference design, with the benefit of reduced overheating. The measure of non-discreteness as presented by Sigmund [60], which serves as a metric for assessing the black-and-white nature of the design, is also relatively low with a value of $M_{\text{nd}} = 3.34\,\%$. This indicates a crisp design with minimal intermediate densities.

3.1. Numerical validation with high-fidelity LPBF process simulation

The effectiveness of the TO schemes in preventing local overheating is assessed using the high-fidelity transient LPBF process simulation described in Section 2.1. Four different cases presented are: i) reference robust TO design given in Fig. 8a, ii) topology optimized design with a geometrical overhang control by Langelaar [4], iii) combined length-scale and overhang control topology

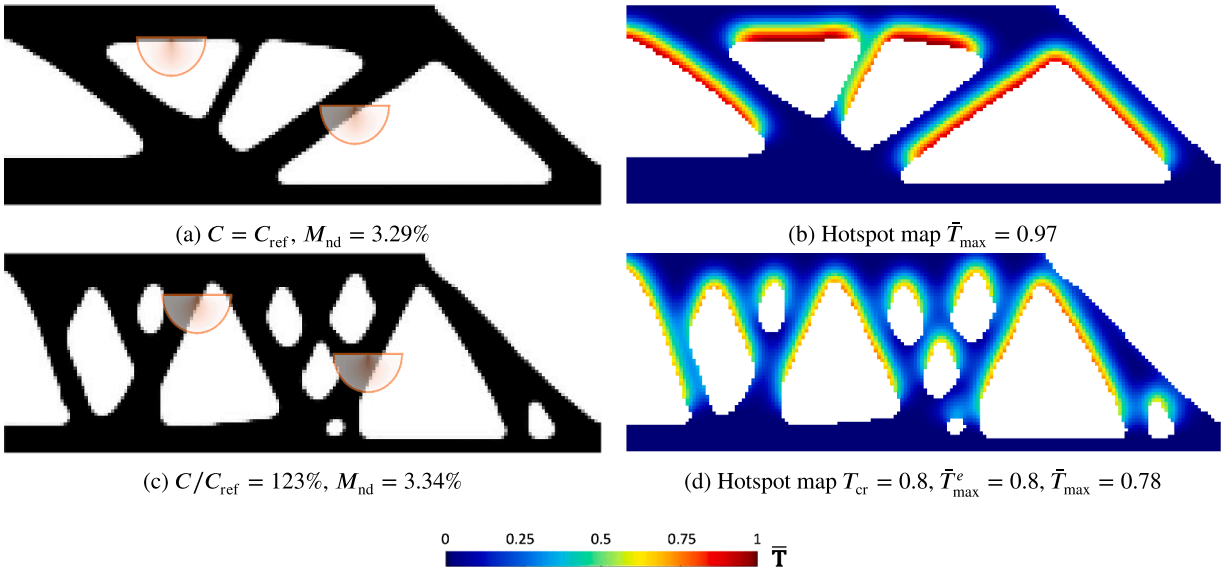

Fig. 8. Robust topology optimized designs (a) without overheating constraint, (c) with overheating constraint, and their corresponding hotspot maps in (b) and (d), respectively. The P-mean scaled maximum at the end of the design iteration is given by $\bar{T}^{e}_{\max}$, and the maximum pseudo-temperature of the hotspot map is given by $\bar{T}_{\max}$. The increase in compliance value compared to the reference design is given by C/C_{ref}, and the measure of non-discreteness is given by M_{nd}.

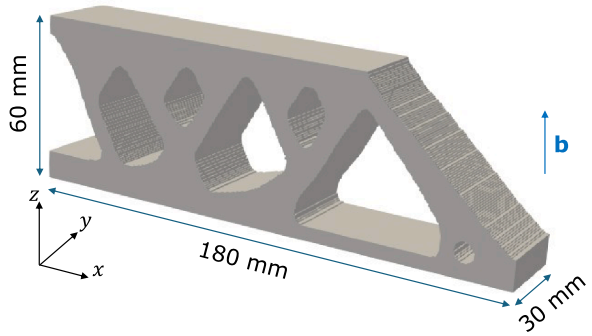

Fig. 9. Part geometry dimensions used for the high-fidelity LPBF process simulation. **b** indicates the build direction.

optimized design by Pellens et al. [61], iv) and the robust TO design with overheating constraint proposed in this paper. All four designs were optimized using a finer resolution of 360×120 elements to achieve good accuracy in the transient thermal simulations. The 2D geometries are extended in the out-of-plane dimension to create 2.5D models for the transient thermal simulations. This enables convenient visualization of temperature fields, as temperatures remain constant along the out-of-plane direction in layer-by-layer simulations. The element size is again taken as 0.5 mm, corresponding to 10 lumped layers for a layer thickness of 50 μm, which makes the domain size of $180\,\text{mm} \times 60\,\text{mm} \times 30\,\text{mm}$. The conductivity domain radius is $\kappa = 12\,\text{mm}$. The build direction is along the z-direction, as shown in Fig. 9.

The maximum temperature field $\mathbf{T}$ during the heating step for all the elements obtained by the high-fidelity model is given in Fig. 10. Also, the spatial average of this temperature field is reported. The maximum temperature indicates the potential overheating risk, while the average of this field assesses overheating regions apart from regions where the maximum temperature occurs. It is evident that the optimized structure without any constraint in Fig. 10a is prone to overheating with $T_{\max} = 1944\,°\text{C}$. This is due to long, almost horizontal overhangs in the design, causing severe overheating. However, constraining the design to have a minimum overhang angle of $\theta_{\text{cr}} = 45°$ does not fully ensure overheating prevention, as shown in Fig. 10b. This is because the funnel-like design features lead to thermal bottlenecks in the design, causing the temperature to rise to a maximum of 1160 °C, as shown in Fig. 10b. The combined length-scale and overhang control TO design eliminates some of these funnel-like structures, reducing the maximum temperature to 1104°, as shown in Fig. 10c. However, with a cost of 24 % compliance increase compared to the reference design. The reduction in performance is due to the length-scale restrictions on solid and void phases, reducing the design freedom.

Since conductivity estimation does not have a provision for overhang angle, to generate a design for comparison, we first perform

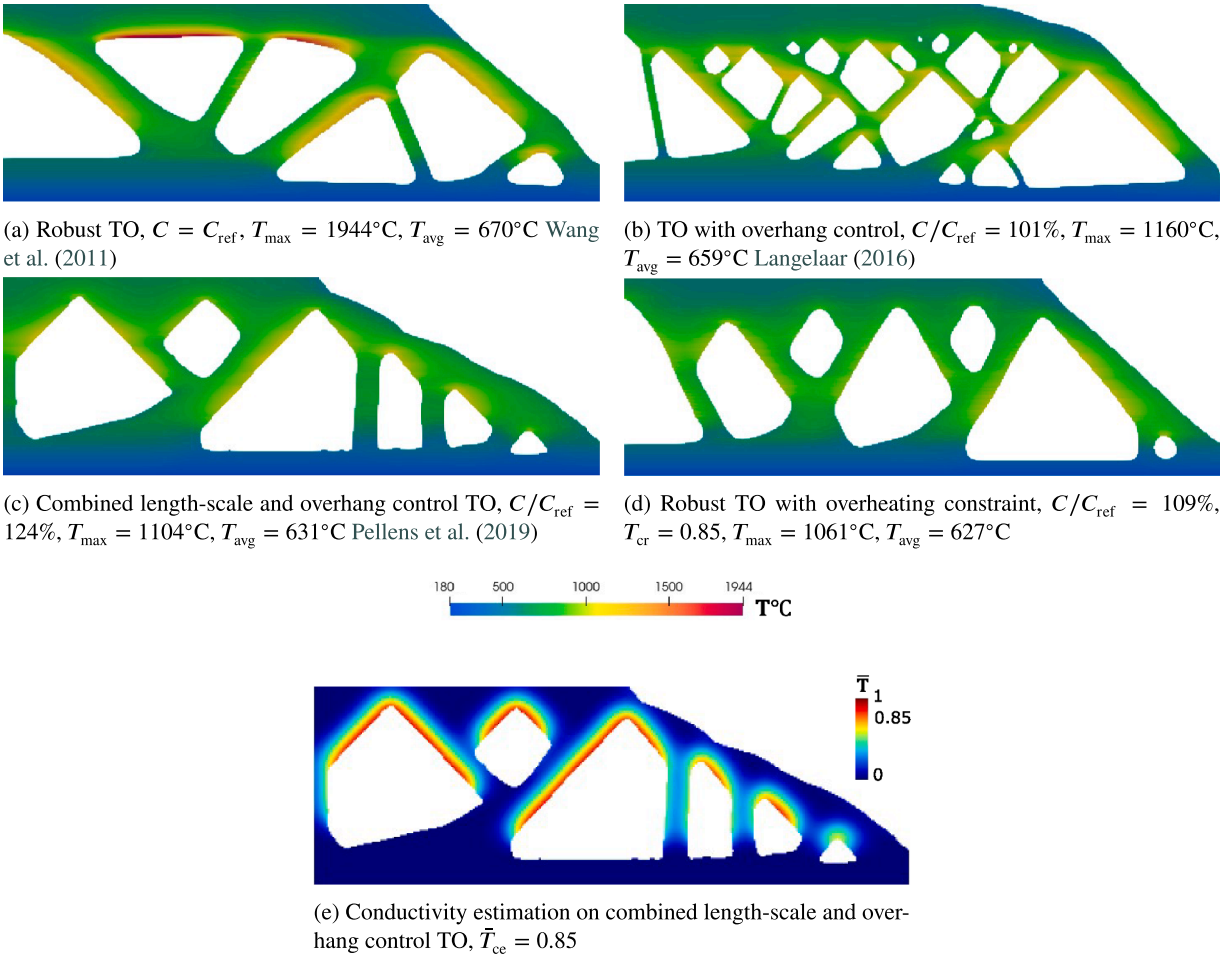

(a) Robust TO, $C = C_{\text{ref}}$, $T_{\max} = 1944°\text{C}$, $T_{\text{avg}} = 670°\text{C}$ Wang et al. (2011)

(b) TO with overhang control, $C/C_{\text{ref}} = 101\%$, $T_{\max} = 1160°\text{C}$, $T_{\text{avg}} = 659°\text{C}$ Langelaar (2016)

(c) Combined length-scale and overhang control TO, $C/C_{\text{ref}} = 124\%$, $T_{\max} = 1104°\text{C}$, $T_{\text{avg}} = 631°\text{C}$ Pellens et al. (2019)

(d) Robust TO with overheating constraint, $C/C_{\text{ref}} = 109\%$, $T_{\text{cr}} = 0.85$, $T_{\max} = 1061°\text{C}$, $T_{\text{avg}} = 627°\text{C}$

(e) Conductivity estimation on combined length-scale and overhang control TO, $\bar{T}_{\text{ce}} = 0.85$

Fig. 10. High-fidelity transient thermal process simulation predictions showing the maximum temperature $T_{\max}$ attained on every material point during the AM process and the spatial average of this field T_{avg} for (a) on a design without any manufacturability constraint, (b) on a design obtained by overhang control, (c) on a design obtained by combined length scale and overhang control, and (d) on a design obtained by the physics-motivated geometric approach. Both (b) and (c) have a critical overhang angle of $\theta_{\text{cr}} = 45°$. The conductivity estimation is used to calculate the maximum hotspot temperature (e) on the robust overhang controlled design as $T_{\text{cr}} = 0.85$ for (d). The increase in compliance value compared to the reference design is given by C/C_{ref}.

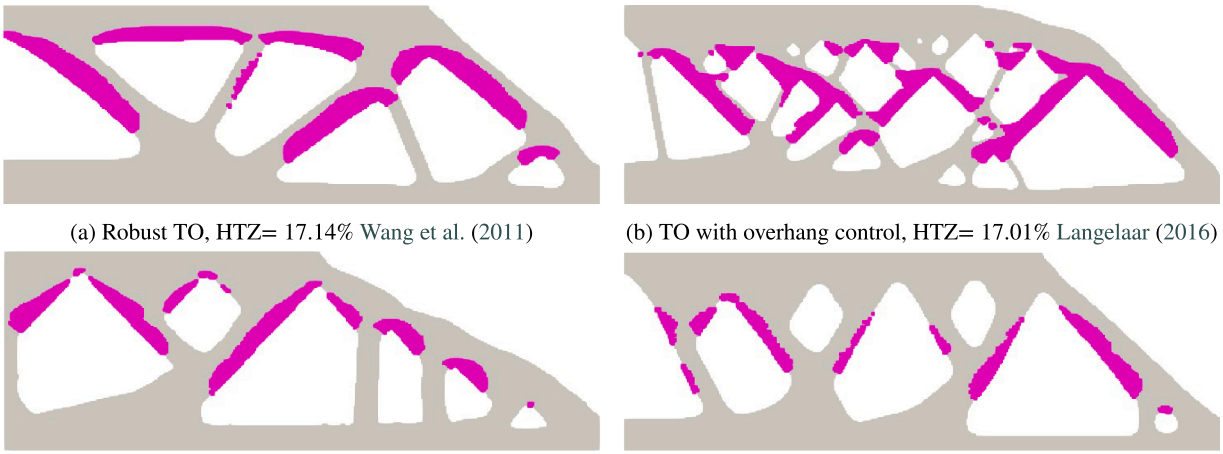

(a) Robust TO, HTZ= 17.14% Wang et al. (2011)

(b) TO with overhang control, HTZ= 17.01% Langelaar (2016)

(c) Combined length-scale and overhang control TO, HTZ= 9.13% Pellens et al. (2019)

(d) Robust TO with overheating constraint, HTZ= 6.03%

Fig. 11. Regions with a maximum temperature $T > 900\,^{\circ}\text{C}$ representing the high-temperature zones (HTZ) highlighted in pink.

a conductivity estimation using Eq. (11) on the combined length-scale and overhang control TO design in Fig. 10c since it is the least overheating prone of the three designs discussed above. The maximum pseudo-temperature $\bar{T}_{\text{ce}} = 0.85$, as shown in Fig. 10e, is considered as the critical temperature T_{cr} in the overheating constraint. Fig. 10d shows the maximum temperature field $\mathbf{T}$ for the proposed conductivity estimation design with $T_{\text{cr}} = 0.85$. The inherent property of the conductivity estimation method to have sufficient material within the conductivity domain generates features that conduct heat efficiently to the baseplate, with a much less compromise on the objective of only 9 %. This is because the conductivity estimation is not restricted to a single critical overhang angle throughout the design, preserving design flexibility, unlike other geometric overhang restrictions for overhangs (e.g. Zhang et al. [2], Langelaar [4], Gaynor et al. [6], Qian [62]) that impose stricter constraints. Also, the temperature field obtained from the high fidelity transient thermal model is depicted in Fig. 10d, where the maximum temperature is only 1061 °C, lower than all other designs shown above. The average temperature of $T_{\text{avg}} = 627$ °C is also lowest among all four designs, indicating a lower spatial maximum temperature distribution. Hence, a physics-motivated geometric representation of heat conduction proposed in this paper establishes a practical balance between overheating control and mechanical performance.

Recall that to quantify the regions of high temperature, we defined high-temperature zones (HTZ), where the temperature is higher than a threshold pseudo-temperature. HTZs indicate the heat accumulation tendencies associated with different geometric features of the AM part. Fig. 11 shows HTZs where the temperature is higher than 85 % ($T > 900$ °C) of the maximum temperature in the conductivity estimation design from Fig. 10d, highlighted with pink. It is important to note that the threshold temperature does not guarantee the absence of local overheating below this value. Instead, it serves as a lower bound to highlight features that are more susceptible to overheating risk. As depicted in Fig. 11a, overhang regions are particularly prone to reach elevated temperatures, with an HTZ volume fraction of 17.14 %. In Fig. 11b, although the maximum temperature is lower, the presence of funnel-like and thin structures hinders effective heat conduction, leading to an HTZ volume fraction of 17.01 %. In the combined length-scale and overhang control TO design, the incorporation of length-scale control enables thicker features, which facilitate more efficient heat dissipation and reduce the HTZ volume fraction to approximately 9.13 %, as shown in Fig. 11c. However, despite the reduced prominence of funnel-like structures compared to the overhang-constrained design in Fig. 11b, the constant degree of overhang still introduces thermal bottlenecks, contributing to gradual heat accumulation in localized regions. The conductivity estimation design is not limited to a uniform overhang angle, allowing for greater design flexibility to create efficient heat conduction pathways. Consequently, the HTZ volume fraction further reduces to 6.03 %, as shown in Fig. 11d. This once again demonstrates that purely geometric control is inadequate for addressing local overheating, emphasizing the need for a physics-based approach to mitigate heat accumulation effectively with more design freedom and higher performance.

The reference robust TO design contains long overhangs, making it unsuitable for printing without the addition of supports. These support structures also serve as heat conduction pathways to the baseplate. To assess how much supports reduce local overheating in the part, we generated tree-like support structures using Autodesk Meshmixer, with a maximum support angle of 45° (consistent with overhang control applied) and a thickness of 3 mm. The high-fidelity transient thermal simulation described above was then applied to the supported design as shown in Fig. 12. The black outline in Fig. 12a and b highlight the boundary between the part and the supports.

The maximum temperature field $\mathbf{T}$ during the heating step, obtained from the high-fidelity model, is shown in Fig. 12a. In our analysis, we focus only on the part itself and exclude the temperatures on the supports. In the supported design, T_{max} in the part decreases from 1944 °C obtained in the unsupported case to 1350 °C, while T_{avg} decreases from 670 °C to 629 °C in the presence of supports. Fig. 12b highlights the high-temperature zones (HTZs), defined as regions above 900 °C. These zones are shown in pink on the part (excluding the supports), while for comparison, the HTZ of the unsupported robust TO design from Fig. 11a is indicated in

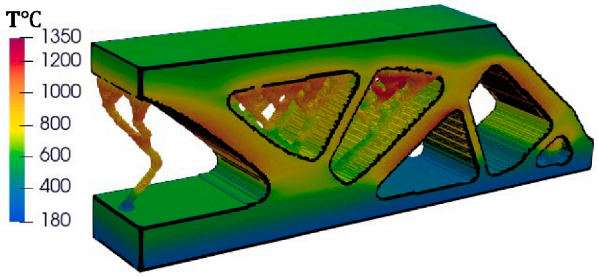

(a) $T_{max} = 1350°C$, $T_{avg} = 629°C$ in the part when supports are excluded.

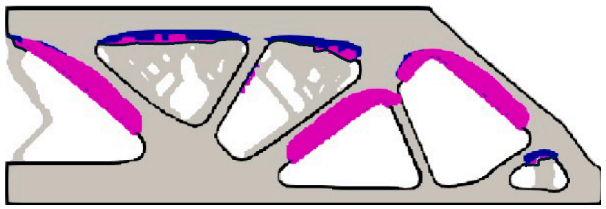

(b) HTZ= 11.42% in the part when supports are excluded.

Fig. 12. Transient high-fidelity thermal simulation showing (a) maximum temperature attained during the AM process on the reference robust TO design with supports and (b) the regions with a maximum temperature $T > 900$ °C representing the high-temperature zones (HTZ) are highlighted in pink. The HTZ for the robust TO design without any supports is superimposed over the supported design and highlighted in dark blue. (For interpretation of the references to color in this figure legend, the reader is referred to the web version of this article.)

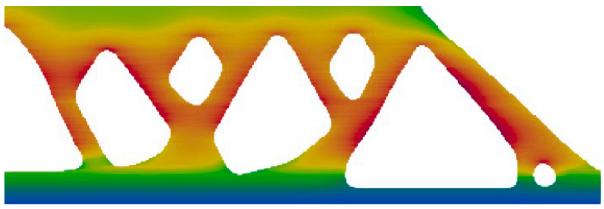

(a) $T_{cr} = 0.85$, $T_{max} = 1061°C$, $T_{avg} = 627°C$, $C/C_{ref} = 109\%$

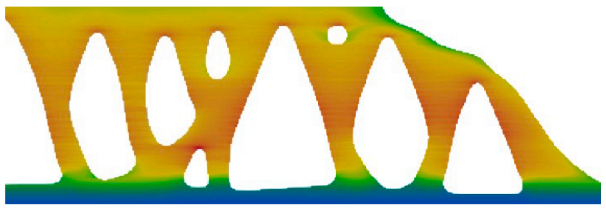

(b) $T_{cr} = 0.70$, $T_{max} = 948°C$, $T_{avg} = 619°C$, $C/C_{ref} = 147\%$

Fig. 13. High-fidelity transient thermal process simulation predictions showing maximum temperature on conductivity estimation designs with different critical temperature T_{cr}.

dark blue. The supported design exhibits an HTZ volume fraction of 11.42 %, compared to 17.14 % in the unsupported case, confirming that supports enhance heat conduction. However, they also increase material consumption, and their removal is both costly and detrimental to surface quality. By contrast, the conductivity estimation design requires no support for manufacturing and thus avoids these drawbacks, while achieving significantly lower values of $T_{max} = 1061$ °C, $T_{avg} = 627$ °C, and HTZ $= 6.03$ %.

Recall that the level of local overheating can be further reduced by choosing a lower T_{cr}. This is demonstrated in Fig. 13, where the transient thermal simulation predictions are superimposed on the designs for $T_{cr} = 0.85$ and $T_{cr} = 0.7$. The maximum temperature **T** during the heating step is compared. With a stricter overheating constraint, the optimizer must add more material inside the conductivity domains such that $\bar{T}^e_{max} = T_{cr}$. As a result, the maximum temperature is just 948 °C and the average temperature is 619 °C. However, this comes at the cost of compromising the objective, resulting in an increase in structural compliance of approximately 47 % for $T_{cr} = 0.70$.

3.2. Extension to 3D

To extend the proposed novel TO method to 3D, we have utilized the standard minimum compliance TO code provided by Liu and Tovar [63]. The code is modified to incorporate robust TO by Wang et al. [57] and our novel overheating constraint. The boundary conditions and loading of the cantilever beam load case are given in Fig. 14. The build direction indicated by **b** is along the z axis. Once again, the reference is the minimum compliance robust TO for a global volume constraint. The conductivity estimation method described in 2D can be extended to 3D by extending the conductivity domain from $\mathbb{R}^2$ to $\mathbb{R}^3$. The conductivity domain hence becomes a hemisphere that encapsulates the solid features in the three-dimensional domain, as shown in Fig. 15a. The orientation of the conductivity domain depends on the build direction to capture the densities of only the elements that are already printed. The weights defined in Section 2.1 account for the proximity to the build direction and the heat source. The grayscale of the conductivity domain indicates the influence of neighboring elements on the local conductivity, i.e., darker shades represent higher influence and vice versa, as shown in Fig. 15a. The local conductivity of every solid element is computed using Eq. (10). Fig. 15b shows the hotspot map generated using Eq. (11) on a topology-optimized design with no overheating constraint. Similar to the 2D cases, heat accumulation occurs in overhanging and thin features, which lack sufficient material beneath them to enable effective heat evacuation.

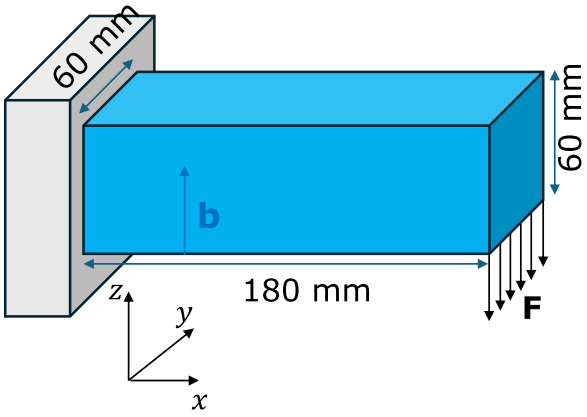

Fig. 14. A 3D cantilever beam problem. The design space, loading, and boundary conditions are given. The cantilever beam has one face fixed, and the load is acting on the bottom front edge. The build direction is indicated by **b**.

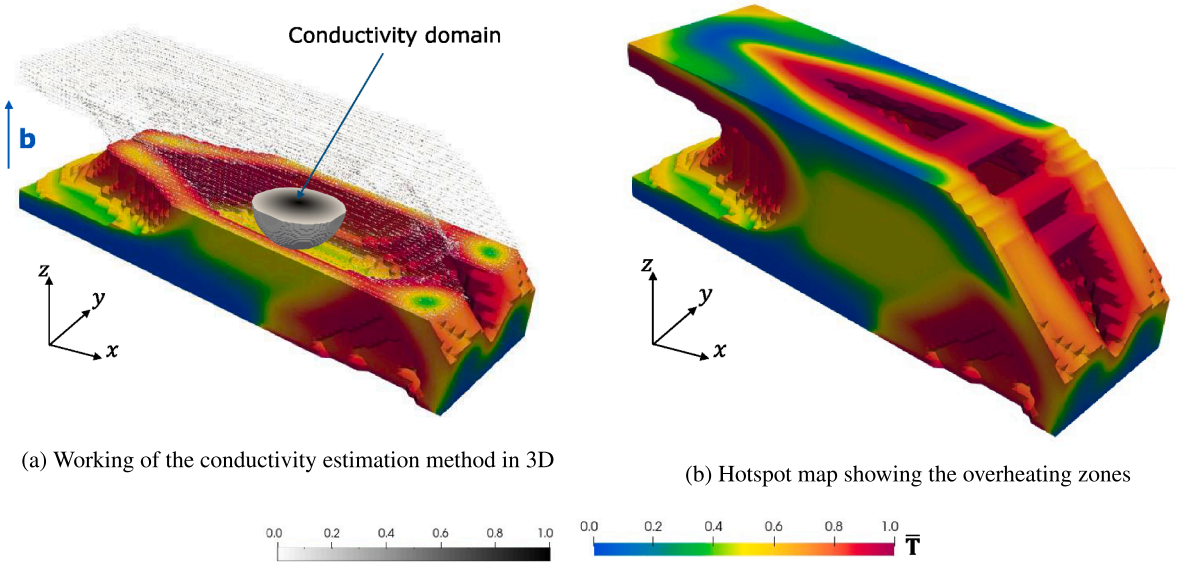

(a) Working of the conductivity estimation method in 3D

(b) Hotspot map showing the overheating zones

Fig. 15. Post optimization hotspot map generated using the conductivity estimation method in 3D robust TO design without the overheating constraint.

Our physics-motivated geometrical overheating constraint and incorporation into the robust TO formulation, as discussed in Section 2.2, can be directly extended to 3D. The critical temperature value is set to $T_{cr} = 0.8$, and two different volume fractions, $v_f = 0.3$ and $v_f = 0.5$, are tested and compared against the robust TO design without the overheating constraint, as shown in Fig. 16. The conductivity domain radius for the given domain size is $\kappa = 14$ mm and $\kappa = 18$ mm for $v_f = 0.3$ and $v_f = 0.5$, respectively. The density filter radius R is one-third of κ, as explained in Section 3. The remaining parameters are taken from Table 1. The design domain is discretized with $90 \times 30 \times 30$ elements. Fig. 16b and d show the hotspot map of the robust TO with the overheating constraint for the volume fraction of 0.3 and 0.5, respectively. The P-mean scaled maximum pseudo-temperature, $\bar{T}^e_{\max} = 0.8$, indicates that both designs satisfy the overheating constraint for $T_{cr} = 0.8$. Also, the maximum pseudo-temperature $\bar{T}_{\max}$ is significantly lower than the $\bar{T}_{\max}$ of reference designs. This is because the overheating constraint redistributes material to ensure adequate heat conduction paths beneath each element, while the length-scale control prevents gaps in the design. Furthermore, the structural compliance exhibits minimal escalation of 7 % and 3 %, for volume fractions of 0.3 and 0.5, respectively.

The cross-sectional view of the designs gives a better idea of the design modifications to limit local overheating, as shown in Fig. 17. Two section views have been taken, one along the $x - z$ plane located halfway along the y axis, called S1, and the second along the $y - z$ plane located halfway along the x axis, S2. The designs without the overheating constraint exhibit severe overheating along the long overhangs, indicating regions with poor heat conduction. This issue is resolved in the designs with the overheating constraint, which introduces sufficient material beneath areas of low heat conduction. Additionally, the teardrop-shaped voids observed in the

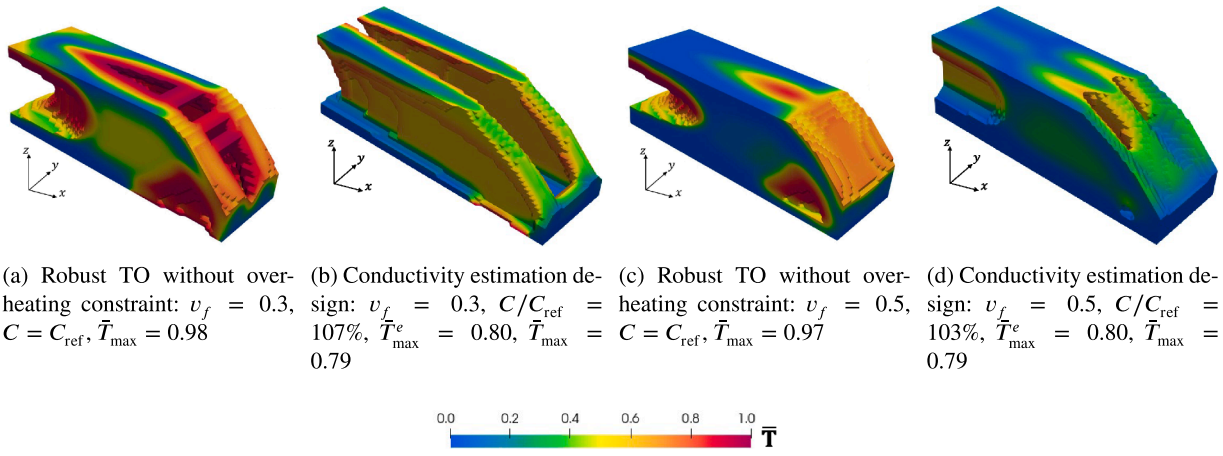

(a) Robust TO without overheating constraint: $v_f = 0.3$, $C = C_{\text{ref}}$, $\bar{T}_{\max} = 0.98$

(b) Conductivity estimation design: $v_f = 0.3$, $C/C_{\text{ref}} = 107\%$, $\bar{T}^e_{\max} = 0.80$, $\bar{T}_{\max} = 0.79$

(c) Robust TO without overheating constraint: $v_f = 0.5$, $C = C_{\text{ref}}$, $\bar{T}_{\max} = 0.97$

(d) Conductivity estimation design: $v_f = 0.5$, $C/C_{\text{ref}} = 103\%$, $\bar{T}^e_{\max} = 0.80$, $\bar{T}_{\max} = 0.79$

Fig. 16. Comparison of the hotspot maps of robust TO for $v_f = 0.3$ (a) without overheating constraint (b) with overheating constraint ($T_{\text{cr}} = 0.8$), and for $v_f = 0.5$ (c) without overheating constraint (d) with overheating constraint ($T_{\text{cr}} = 0.8$). The P-mean scaled maximum at the end of the design iteration is given by $\bar{T}^e_{\max}$, and the maximum pseudo-temperature of the hotspot map is given by $\bar{T}_{\max}$. The increase in compliance value compared to the reference design is given by C/C_{ref}.

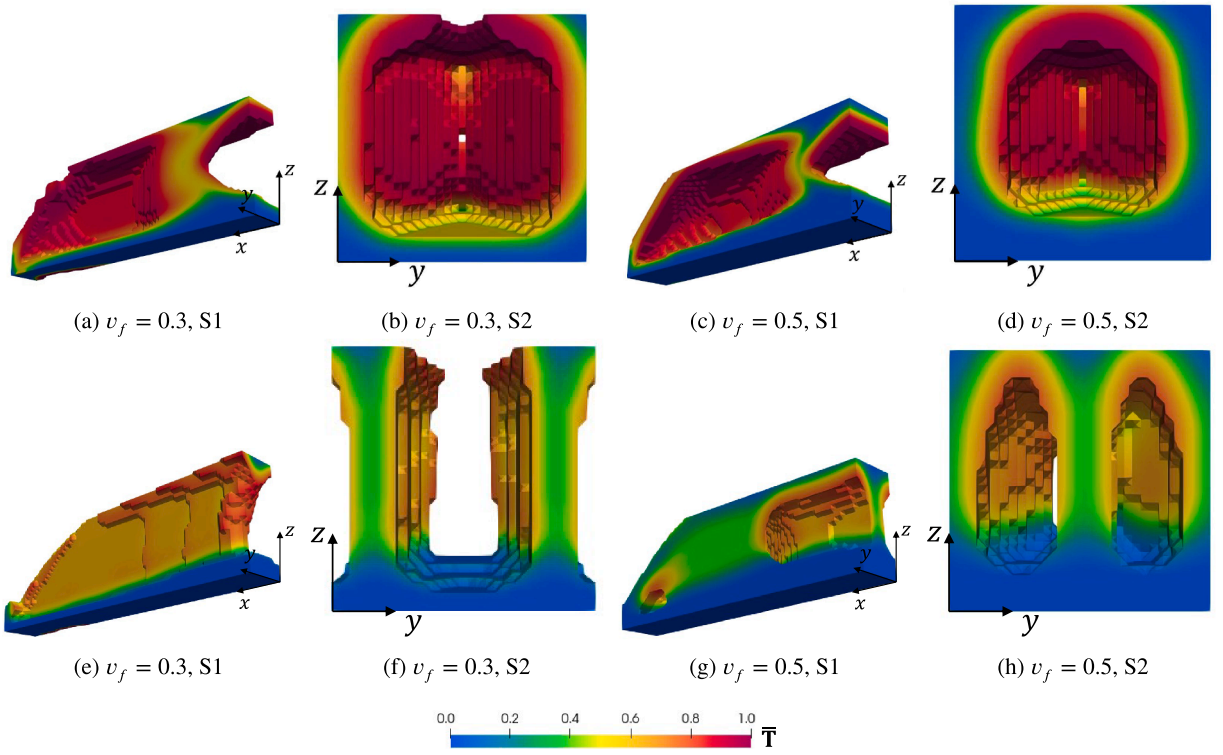

(a) $v_f = 0.3$, S1

(b) $v_f = 0.3$, S2

(c) $v_f = 0.5$, S1

(d) $v_f = 0.5$, S2

(e) $v_f = 0.3$, S1

(f) $v_f = 0.3$, S2

(g) $v_f = 0.5$, S1

(h) $v_f = 0.5$, S2

Fig. 17. Section views of the designs obtained with and without the overheating constraint. Section views 1 and 2 of the robust TO for $v_f = 0.3$ are shown in (a) and (b), respectively, and for $v_f = 0.5$, in (c) and (d), respectively. Section views 1 and 2 of the conductivity estimation design for $v_f = 0.3$ are shown in (e) and (f), respectively, and for $v_f = 0.5$, in (g) and (h), respectively.

2D designs appear in the 3D problem, as shown in Fig. 17f and h. Hence, the conductivity estimation designs effectively mitigate features that lead to local overheating, while maintaining structural stiffness with minimal compromise in 3D TO problems.

3.3. Computational cost comparison

The computation times of all four designs mentioned in Section 3.1 and the physics-based local overheating reduction method by Ranjan et al. [39] are compared, considering a design domain of 360×120 elements in 2D. The wall clock times are measured on a 3 GHz processor with 16 GB of RAM. Moreover, the computation times of conductivity estimation in 3D explained in Section 3.2 and the physics-based local overheating reduction method in 3D by Ranjan et al. [40] are also presented to show the computational efficiency of our physics-motivated geometric method as compared to a physics-based overheating reduction method. In the 3D setting, a domain size resolution of $120 \times 40 \times 40$ elements is used, and simulations are performed on an HPC cluster. The wall clock time of the simulations, including computational operations and system overhead, is given in Fig. 18a and b for the designs in 2D and 3D, respectively. Table 2 shows the average wall-clock time per iteration for 2D and 3D.

The computation time of the robust TO design is taken as a reference. In 2D, the computational cost of TO with overhang control is relatively low. The adjoint approach involves simple operations with sparse or even diagonal matrices per layer, which makes the order of complexity as $O(N)$, where N is the total number of elements in the design domain. The computational cost doesn't increase significantly in the combined length-scale and overhang control, as only the eroded design densities are considered for the compliance calculation. In the conductivity estimation method, the conductivity of each element i depends on $j \in S_i$ in the conductivity domain, and thus, the sensitivity analysis includes densely populated sparse matrix multiplication (see Appendix A.4). Hence, the order of complexity is now $O(Nd^2)$, where d is the number of non-zero elements per row of the sparse matrix. However, the computation time is still significantly lower than the physics-based hotspot reduction method [39,40]. This is because in the latter, solving even a steady-state heat equation over a smaller sub-domain has a complexity of order $O(N^3)$, where N is the degrees of freedom in the sub-domain, and multiple such steady-state thermal equations are solved along the build direction, increasing the computation time significantly. Additionally, in the conductivity estimation method, the weight functions can be pre-computed outside the iteration loop, similar to the density filter by Bruns and Tortorelli [54]. As seen from Table 2, the computation time per iteration of the geometric conductivity

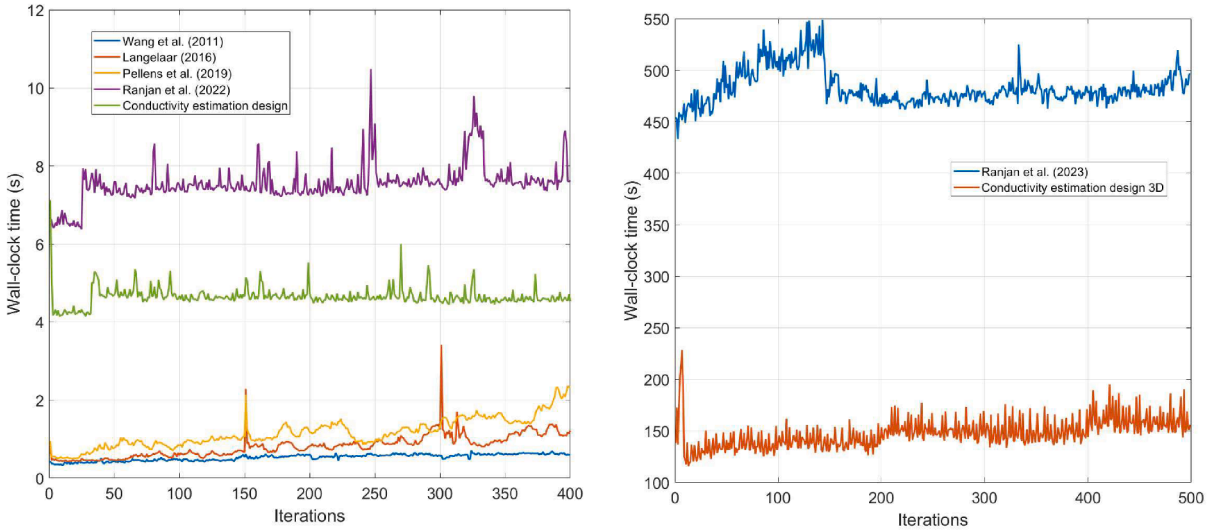

(a) Computation times in 2D (from top to bottom in legend) robust TO, TO with overhang control, combined length-scale and overhang control TO, TO with physics-based hotspot constraint, conductivity estimation design.

(b) Computation times in 3D (from top to bottom in legend) TO with physics-based hotspot constraint, conductivity estimation design.

Fig. 18. Computation times over the iterations for different optimization methods in 2D and 3D.

Table 2
Average CPU time per iteration for different TO designs.

Models	CPU time (s)/iteration 2D	CPU time (s)/iteration 3D
Robust TO [57]	0.59	–
TO with overhang control [4]	0.83	–
Combined length-scale and overhang control TO [61]	1.42	–
TO with physics-based hotspot constraint [39,40]	7.54	483.04
Robust TO with overheating constraint	4.78	147.82

estimation method is around 1.58 times lower than the physics-based hotspot constraint. The reduction in time is more prominent in 3D, where the degrees of freedom increase, and we see a significant reduction of around 3.26 times compared to the physics-based method by Ranjan et al. [40]. Thus, the conductivity estimation method proved to be computationally efficient in reducing local overheating compared to the physics-based methods.

4. Conclusions

A novel geometric yet physics-motivated hotspot detection method and its integration with the TO are presented to address the local overheating prevention in metal AM. The method uses a geometric representation of heat conduction and computes a local conductivity measure for all the material points in the design domain. The weight factors used ensure that the physics of heat conduction is incorporated in the computation of the local conductivity. A comparison with high-fidelity transient thermal simulation revealed that the conductivity estimation method can detect critical overheating zones in the part very efficiently. The conductivity estimation method is employed as an overheating constraint in robust TO. The constraint is formulated to remain active in regions with poor heat conduction and is easily satisfied elsewhere. As a result, the overheating constraint compels the optimizer to modify the density in low-conduction regions to create heat conduction paths to the baseplate and reduce the risk of overheating.

The designs obtained using the overheating constraint with robust TO proved superior in avoiding local overheating when analyzed with a high-fidelity transient thermal AM simulation and compared against geometric TO designs. Strictly restricting overhang inclination can still lead to AM manufacturability challenges, especially when long overhangs taper into thinner features, creating thermal bottlenecks. Combined length-scale overhang-controlled designs mitigate local overheating by incorporating thicker features, which allow for improved heat evacuation. However, the trade-off with this approach is a notable decrease in the structural performance. On the contrary, the conductivity estimation method does not directly constrain the overhang angle to a fixed value, increasing the design freedom and leading to better structural performance and overheating prevention. The decrease in stiffness is even lower in 3D than in 2D, indicating that designs free from local overheating can be achieved without compromising structural integrity for large TO problems. Moreover, a significant computational gain is obtained for finer resolution geometries and large 3D structures with the geometric conductivity estimation method compared to other physics-based local overheating prevention methods in the literature.

The critical temperature value, T_{cr}, is introduced as a tunable parameter that enables improved overheating prevention at the cost of reduced stiffness. It is up to the user to find the trade-off between compliance and overheating reduction by tuning the critical temperature value. Determining its appropriate value for a given material and process parameters is beyond the scope of this paper. Furthermore, developing a framework to define the weight functions of the conductivity domain based on these parameters is essential for enhancing the optimized designs. At present, the conductivity estimation method is limited to planar layer deposition. The next step involves modifying the conductivity domain to align with the build direction and the curvature of the deposition layers, thereby incorporating the fabrication sequence in nonplanar material deposition, an approach made feasible through robot-assisted multi-axis AM.

CRediT authorship contribution statement

Manabendra Nath Das: Writing – original draft, Visualization, Supervision, Software, Methodology, Investigation, Data curation, Conceptualization; **Rajit Ranjan:** Writing – review & editing, Supervision, Data curation, Conceptualization; **Kai Wu:** Writing – review & editing, Supervision, Conceptualization; **Jun Wu:** Writing – review & editing, Supervision, Data curation, Conceptualization; **Can Ayas:** Writing – review & editing, Supervision, Data curation, Conceptualization.

Data availability

Data will be made available on request.

Declaration of competing interest

The authors declare that they have no known competing financial interests or personal relationships that could have appeared to influence the work reported in this paper.

Acknowledgements

This work is partly supported by the Dutch Research Council (NWO), Netherlands, with project number 20382, “Space–time optimization for additive manufacturing”.

Appendix A.

A.1. Influence of conductivity penalization q and relaxation exponent r

We perform a parameter sweep to identify suitable values for the conductivity penalization exponent $q = 1, 3, 5$ in Eq. (10) and the relaxation exponent $r = 0.01, 0.05, 0.1, 0.25, 0.5$ in Eq. (19d), as summarized in Fig. A.19. All other parameters are taken

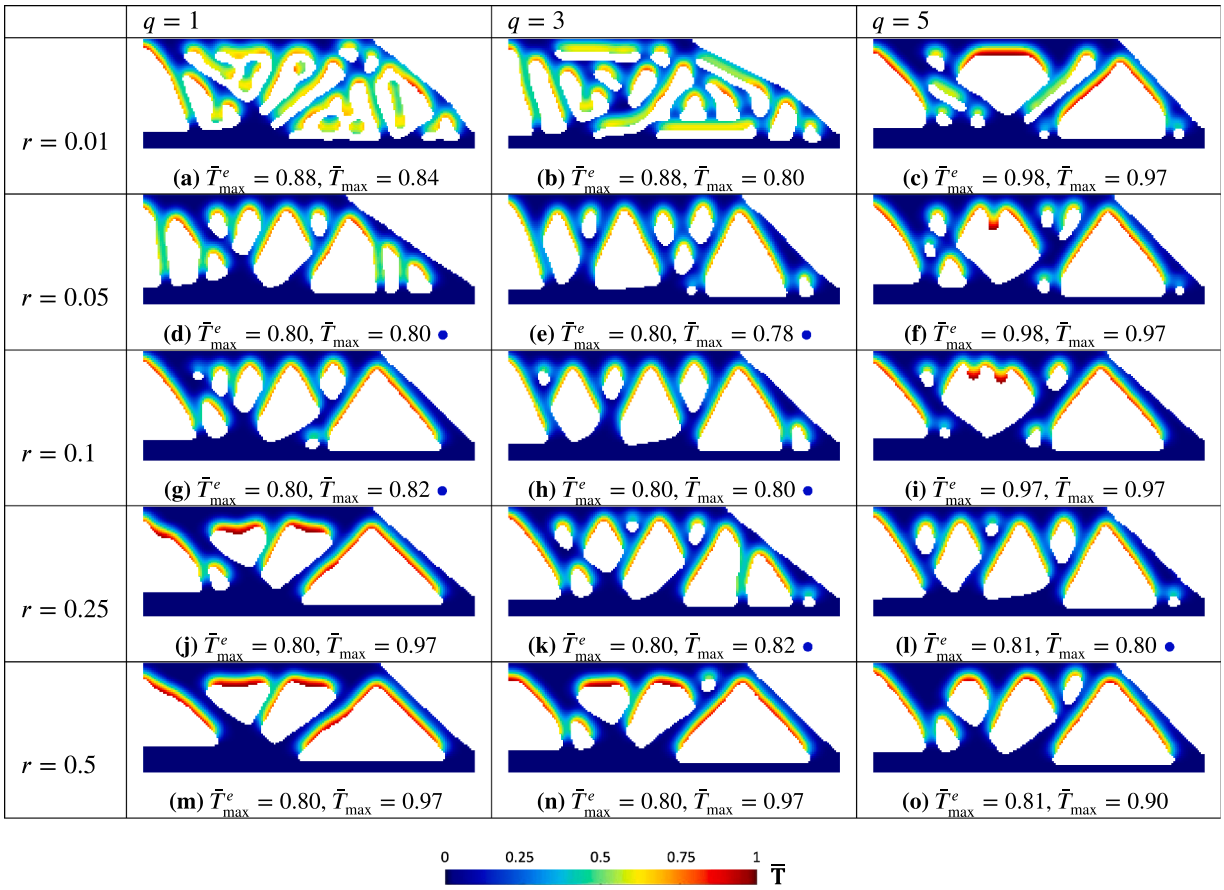

Fig. A.19. Parametric sweep of conductivity penalization q and relaxation exponent r for $T_{cr} = 0.8$. The P-mean scaled maximum at the end of the design iteration is given by $\bar{T}^e_{\max}$, and the maximum pseudo-temperature of the hotspot map is given by $\bar{T}_{\max}$. The blue dot indicates the feasible designs obtained. (For interpretation of the references to color in this figure legend, the reader is referred to the web version of this article.)

from Table 1, with the critical temperature value fixed at $T_{cr} = 0.8$. Designs that are both feasible and effective in suppressing local overheating are marked with a blue dot next to their respective captions. The parameter q controls the degree of penalization applied to intermediate densities: higher values lead to stronger penalization. The parameter r influences the required value of $\bar{\mu}$ to meet the critical temperature value T_{cr}: larger r values reduce the required $\bar{\mu}$, resulting in fewer solid elements in the conductivity domain.

When r is very low (e.g., $r = 0.01$), the required $\bar{\mu}$ becomes excessively high to satisfy the constraint. As shown in Fig. A.19a–c, this causes solid densities to cluster, leading to infeasible designs. On the other hand, very high r values (e.g., $r = 0.5$) result in lower required $\bar{\mu}$ values to satisfy the overheating constraint following Eq. (19d) and exemplified by designs shown in Fig. A.19m–o. However, these designs still turn out to be infeasible, as their maximum pseudo-temperatures of the hotspot map $\bar{T}_{\max}$ exceed the threshold, despite $\bar{T}^e_{\max} = T_{cr}$.

The penalization exponent q helps avoid intermediate densities in the local conductivity calculation. However, its impact is most relevant during the early optimization iterations when the projection sharpness β is low. If the penalization is too strong (e.g., $q = 5$), intermediate densities are quickly eliminated, and the design prematurely converges to a black-and-white configuration before β is increased. This premature convergence makes it difficult for the optimizer to update the design variables and satisfy the constraints, as illustrated in Fig. A.19o, i, f, c. The only exception is shown in Fig. A.19l, where a lower required $\bar{\mu}$ allows the design to converge even with high penalization. In contrast, the designs shown in Fig. A.19d, g, e, h, k exhibit good convergence and successfully satisfy the imposed constraints. Since $q = 1$ leads to convergence issues at higher r values (see Fig. A.19j), the recommended choice is $q = 3$, as it allows for a broader usable range of r values.

A.2. Influence of critical temperature T_{cr} and relaxation exponent r

A parametric sweep of the critical temperature value $T_{cr} = 0.9, 0.8, 0.7$ in the overheating constraint given in Eq. (19d) is performed for different relaxation exponent values $r = 0.01, 0.05, 0.1, 0.25, 0.5$ to investigate how the strictness of the constraint influences the resulting designs, as shown in Fig. A.20. All parameters are consistent with those in Table 1, except for the number of iterations for the β update cycle and constraint scaling parameter c_0. As the overheating constraint becomes stricter, more iterations are required

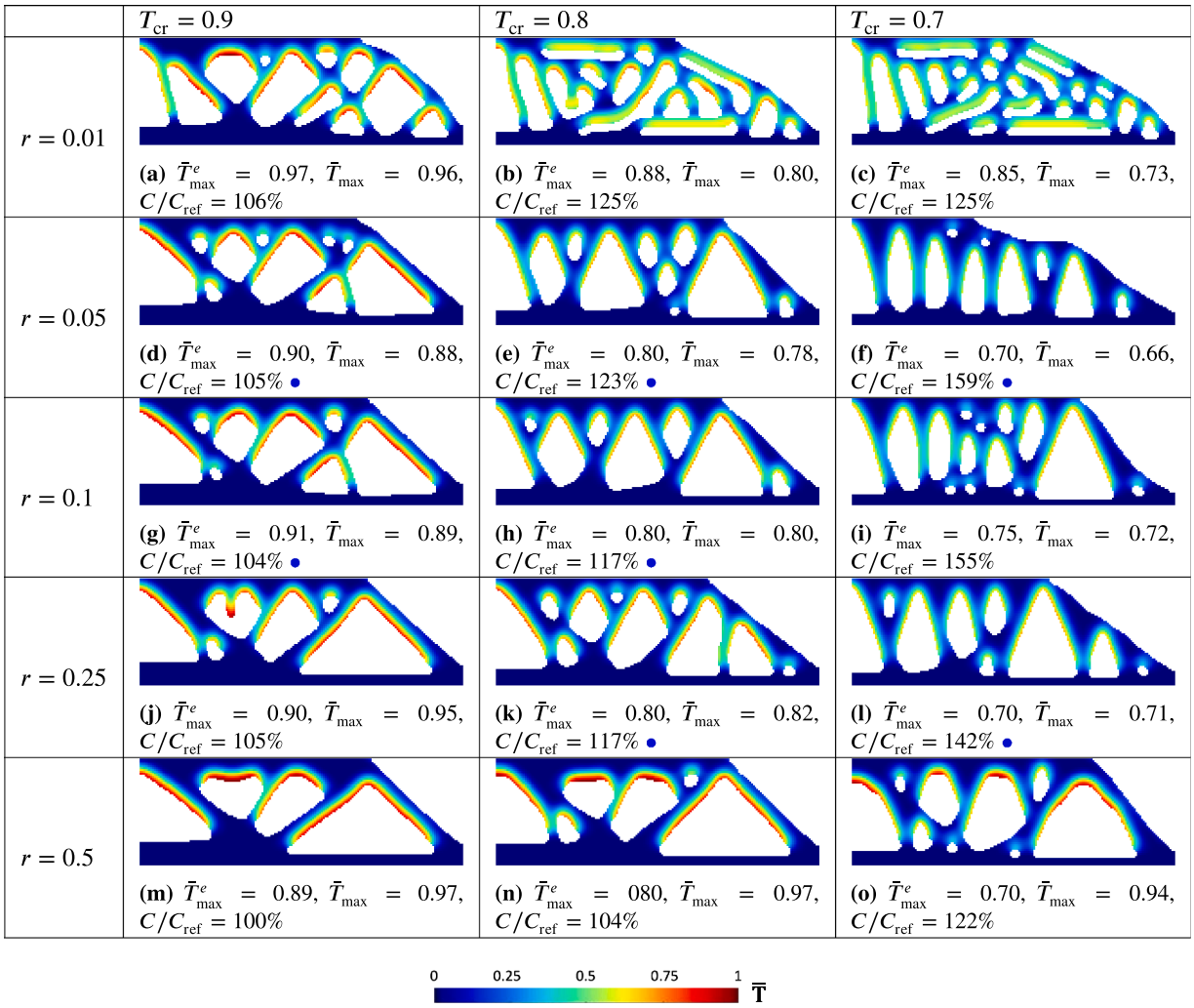

Fig. A.20. Parametric sweep of critical temperature T_{cr} and relaxation exponent r for $q = 3$. The P-mean scaled maximum at the end of the design iteration is given by $\bar{T}^e_{max}$, and the maximum pseudo-temperature of the hotspot map is given by $\bar{T}_{max}$. The increase in compliance value compared to the reference design is given by C/C_{ref}. The blue dot indicates the feasible designs obtained. (For interpretation of the references to color in this figure legend, the reader is referred to the web version of this article.)

for convergence, necessitating a slower update of β. Specifically, β is updated every 50 iterations for $T_{cr} = 0.9$, every 100 iterations for $T_{cr} = 0.8, 0.7$. Additionally, the values of $c_0 = 1000, 2500, 3500$ for $T_{cr} = 0.9, 0.8, 0.7$, respectively, showed good convergence behaviour.

As in the previous study from Appendix A.1, infeasible designs are observed at both very low and very high values of r, as shown in Fig. A.20c, b, a, o, n, m, respectively. When T_{cr} is lowered, the constraint becomes more stringent, prompting the addition of more solid material beneath each element to lower the P-mean scaled maximum pseudo-temperature $\bar{T}^e_{max}$. These solid regions often form nearly vertical features that ensure direct thermal conduction paths from the topmost layers to the baseplate, enabling efficient heat evacuation. Additionally, thinner features tend to be straighter than thicker ones due to limited material availability for heat conduction. Funnel-shaped structures that cause thermal bottlenecks and are observed at higher T_{cr} values vanish as the constraint tightens. This transition gives rise to tear-drop-shaped voids, which resemble those seen in physics-based hotspot-constrained topology-optimized designs reported by Ranjan et al. [39]. However, as design freedom decreases under stricter constraints, structural compliance increases. Conversely, increasing r leads to greater design freedom by reducing the required $\bar{\mu}$ to meet the overheating constraint, which in turn lowers compliance, as observed in Fig. A.20f, i, l.

The designs obtained for different T_{cr} values perform well within the previously identified optimal range of $r = 0.05, 0.1, 0.25$, with a few exceptions noted in Fig. A.20j, i. Among these, $r = 0.05$ consistently yields feasible designs for all values of T_{cr}, as demonstrated in Fig. A.20f, e, d, and is therefore recommended. However, if both better stiffness and improved overheating control are desired, higher values of r may be preferred for stricter T_{cr}, as illustrated in Fig. A.20d, h, l.

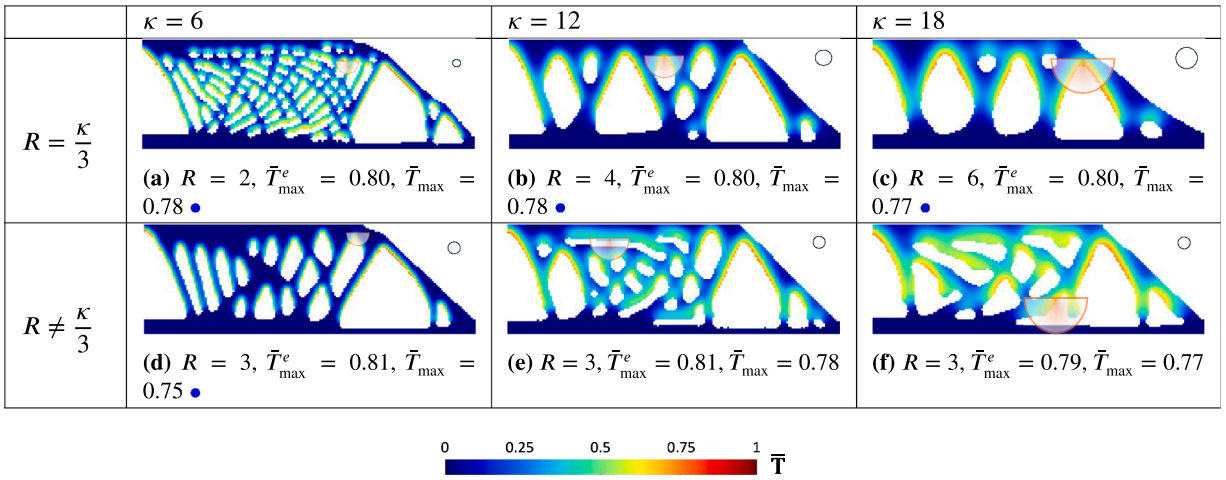

Fig. A.21. Parametric sweep of density filter radius R and conductivity domain radius κ for $T_{cr} = 0.8$. The P-mean scaled maximum at the end of the design iteration is given by $\bar{T}^e_{max}$, and the maximum pseudo-temperature of the hotspot map is given by $\bar{T}_{max}$. The blue dot indicates the feasible designs obtained. (For interpretation of the references to color in this figure legend, the reader is referred to the web version of this article.)

A.3. Influence of density filter radius R on the conductivity domain radius κ

The conductivity domain radius κ controls the domain size in calculating the local conductivity. In 2D, a conductivity domain radius of $\kappa = 12$ mm has been used in all simulations, as this corresponds to the thermal interaction length derived from our process parameters and material properties, following the method outlined in Ranjan et al. [32]. To examine the influence of the density filter radius R and the parameter κ on the conductivity estimation designs, simulations are conducted using $\kappa = 6,\ 12,\ 18$ mm, with varying values of R, for $T_{cr} = 0.8$, as summarized in Fig. A.21. In the figures, the conductivity domain is represented by an orange semicircle, while the density filtering domain is shown as a black circle. In the first row, R is set to one-third of κ, whereas in the second row, it is assigned a value of $\kappa/2, \kappa/4$, and $\kappa/6$.

Feasible designs are obtained when R corresponds to one-third of κ as seen in Fig. A.21a, b, c. This is because the density filter radius in the robust TO projection is adequate to enforce a length scale in both solid and void phases. An improvement is observed when the ratio of R/κ is increased to 1/2, as shown in Fig. A.21a, where the design is free from the smaller void regions seen in Fig. A.21a. This results in more efficient pathways for heat conduction. However, choosing a smaller ratio of 1/4 or 1/6 can result in gaps existing in the final design as the density filtering domain is insufficient to impose a length scale for the features inside the conductivity domain, as seen in Fig. A.21e, f. Even though they satisfy the overheating constraint as indicated by $\bar{T}^e_{max}$, and the maximum pseudo temperature from the hotspot map $\bar{T}_{max}$ is below 0.8, these gaps will result in local overheating. Therefore, selecting an appropriate value of κ, based on material properties and process parameters, and the corresponding R, is crucial for controlling the design features in the proposed overheating constraint TO.

A.4. Sensitivity analysis of the overheating constraint

The overheating constraint given by Eq. (19d) is differentiated with respect to the eroded projected densities $\bar{\tilde{\rho}}^e$ to calculate its sensitivity. The partial derivative $\frac{\partial g}{\partial \bar{\tilde{\rho}}^e_l}$ is a result of sparse matrix multiplication. The non-zero entries in the sparse matrix are due to the dependence of each element l on the conductivity domain of other elements. Let this set of elements be denoted as $k \in P_l$, where element l exists in the conductivity domain of the k^{th} element. To represent this relationship, we define a sparse matrix Ψ of size $N \times N$, where the non-zero entries in row i correspond to indices $j \in S_i$, representing elements in the conductivity domain of element i. Conversely, the elements k for which element l lies in their conductivity domain can be identified as the non-zero entries in row l of the transpose matrix Ψ^{T}. Thus, the sensitivity of the overheating constraint $\frac{\partial g}{\partial \bar{\tilde{\rho}}_l}$ (superscript e removed for brevity) is evaluated as follows:

$$\frac{\partial g}{\partial \bar{\tilde{\rho}}_l} = \frac{\alpha}{N T_{cr}} \left[\frac{1}{N} \sum_{i=1}^{N} \left((1-\bar{\mu}_i)\bar{\tilde{\rho}}^r_i \right)^P \right]^{\frac{1}{P}-1} \sum_{k \in P_l} \left[\left((1-\bar{\mu}_k)\bar{\tilde{\rho}}^r_k \right)^{P-1} \left(r(1-\bar{\mu}_k)\bar{\tilde{\rho}}^{r-1}_k \delta_{kl} - \frac{q\bar{\tilde{\rho}}^r_k \bar{\tilde{\rho}}^{q-1\,k}_l w_l}{\sum_{j \in S_k}{}^k w_j} \right) \right]. \tag{20}$$

Sensitivities with respect to the design variables are calculated using the chain rule as:

$$\frac{\partial g}{\partial \rho} = \frac{\partial g}{\partial \bar{\tilde{\rho}}} \frac{\partial \bar{\tilde{\rho}}}{\partial \tilde{\rho}} \frac{\partial \tilde{\rho}}{\partial \rho}. \tag{21}$$

References

[1] E. van de Ven, R. Maas, C. Ayas, M. Langelaar, F. van Keulen, Overhang control based on front propagation in 3D topology optimization for additive manufacturing, Comput. Methods Appl. Mech. Eng. 369 (2020) 113169.
[2] K. Zhang, G. Cheng, L. Xu, Topology optimization considering overhang constraint in additive manufacturing, Comput. Struct. 212 (2019) 86–100.
[3] A. Garaigordobil, R. Ansola, J. Santamaría, I. Fernández de Bustos, A new overhang constraint for topology optimization of self-supporting structures in additive manufacturing, Struct. Multidiscip. Optim. 58 (2018) 2003–2017.
[4] M. Langelaar, Topology optimization of 3D self-supporting structures for additive manufacturing, Addit. Manuf. 12 (2016) 60–70.
[5] J. Wu, C.C.L. Wang, X. Zhang, R. Westermann, Self-supporting rhombic infill structures for additive manufacturing, Computer-Aided Des. 80 (2016) 32–42.
[6] A.T. Gaynor, N.A. Meisel, C.B. Williams, J.K. Guest, Topology optimization for additive manufacturing: considering maximum overhang constraint, in: 15th AIAA/ISSMO Multidisciplinary Analysis and Optimization Conference, 2014, p. 2036.
[7] G. Misiun, E. van de Ven, M. Langelaar, H. Geijselaers, F. van Keulen, T. van den Boogaard, C. Ayas, Topology optimization for additive manufacturing with distortion constraints, Comput. Methods Appl. Mech. Eng. 386 (2021) 114095.
[8] T. Miki, T. Yamada, Topology optimization considering the distortion in additive manufacturing, Finite Elem. Anal. Des. 193 (2021) 103558.
[9] R.A. Wildman, A.T. Gaynor, Topology optimization for reducing additive manufacturing processing distortions, Weapons and Materials Research Directorate, US Army Research Laboratory Aberdeen Proving Ground United States (2017).
[10] S. Xu, J. Liu, Y. Ma, Residual stress constrained self-support topology optimization for metal additive manufacturing, Comput. Methods Appl. Mech. Eng. 389 (2022) 114380.
[11] L. Cheng, X. Liang, J. Bai, Q. Chen, J. Lemon, A. To, On utilizing topology optimization to design support structure to prevent residual stress induced build failure in laser powder bed metal additive manufacturing, Addit. Manuf. 27 (2019) 290–304.
[12] G. Allaire, L. Jakabčin, Taking into account thermal residual stresses in topology optimization of structures built by additive manufacturing, Math. Models Methods Appl. Sci. 28 (12) (2018) 2313–2366.
[13] R. Mertens, S. Clijsters, K. Kempen, J.-P. Kruth, Optimization of scan strategies in selective laser melting of aluminum parts with downfacing areas, J. Manuf. Sci. Eng. 136 (6) (2014) 061012.
[14] W.J. Sames, F.A. List, S. Pannala, R.R. Dehoff, S.S. Babu, The metallurgy and processing science of metal additive manufacturing, Int. Mater. Rev. 61 (5) (2016) 315–360.
[15] T. Craeghs, S. Clijsters, J.-P. Kruth, F. Bechmann, M.-C. Ebert, Detection of process failures in layerwise laser melting with optical process monitoring, Phys. Procedia 39 (2012) 753–759.
[16] L.A. Parry, I.A. Ashcroft, R.D. Wildman, Geometrical effects on residual stress in selective laser melting, Addit. Manuf. 25 (2019) 166–175.
[17] D. Kastsian, D. Reznik, Reduction of local overheating in selective laser melting, Simulation for Additive Manufacturing Sim-AM, Munich (2017).
[18] R. Leach, S. Carmignato, Precision Metal Additive Manufacturing, CRC Press, 2020.
[19] T. Craeghs, F. Bechmann, S. Berumen, J.-P. Kruth, Feedback control of layerwise laser melting using optical sensors, Phys. Procedia 5 (2010) 505–514.
[20] V. Mishra, C. Ayas, M. Langelaar, Design for material properties of additively manufactured metals using topology optimization, Mater. Des. 235 (2023) 112388.
[21] V. Mishra, A. Babu, R. Schreurs, K. Wu, M. Hermans, C. Ayas, Microstructure estimation and validation of ER110S-G steel structures produced by wire and arc additive manufacturing, J. Mater. Res. Technol. 23 (2023) 3579–3601.
[22] M. Leary, M. McMillan, D. Shidid, H. VanToor, M. Mazur, M. Brandt, Numerical methods to predict overheating in SLM lattice structures, in: International Congress on Applications of Lasers & Electro-Optics, AIP Publishing, 2014, pp. 895–902.
[23] L. Thijs, F. Verhaeghe, T. Craeghs, J. Van Humbeeck, J.-P. Kruth, A study of the microstructural evolution during selective laser melting of Ti–6Al–4V, Acta Mater. 58 (9) (2010) 3303–3312.
[24] M. Rombouts, L. Froyen, A.V. Gusarov, E.H. Bentefour, C. Glorieux, Photopyroelectric measurement of thermal conductivity of metallic powders, J. Appl. Phys. 97 (2) (2005).
[25] J. Romano, L. Ladani, M. Sadowski, Thermal modeling of laser based additive manufacturing processes within common materials, Procedia Manuf. 1 (2015) 238–250.
[26] J. Jiang, J. Stringer, X. Xu, R.Y. Zhong, Investigation of printable threshold overhang angle in extrusion-based additive manufacturing for reducing support waste, Int. J. Computer Integr. Manuf. 31 (10) (2018) 961–969.
[27] M. Cloots, A.B. Spierings, K. Wegener, Assessing new support minimizing strategies for the additive manufacturing technology SLM, in: 2013 International Solid Freeform Fabrication Symposium, University of Texas at Austin, 2013.
[28] D. Wang, Y. Yang, Z. Yi, X. Su, Research on the fabricating quality optimization of the overhanging surface in SLM process, Int. J. Adv. Manuf. Technol. 65 (2013) 1471–1484.
[29] J. Liu, A.T. Gaynor, S. Chen, Z. Kang, K. Suresh, A. Takezawa, L. Li, J. Kato, J. Tang, C.C.L. Wang, et al., Current and future trends in topology optimization for additive manufacturing, Struct. Multidiscip. Optim. 57 (6) (2018) 2457–2483.
[30] M. Langelaar, An additive manufacturing filter for topology optimization of print-ready designs, Struct. Multidiscip. Optim. 55 (2017) 871–883.
[31] G.A.O. Adam, D. Zimmer, Design for additive manufacturing—Element transitions and aggregated structures, CIRP J. Manuf. Sci. Technol. 7 (1) (2014) 20–28.
[32] R. Ranjan, C. Ayas, M. Langelaar, F. van Keulen, Fast detection of heat accumulation in powder bed fusion using computationally efficient thermal models, Materials 13 (20) (2020) 4576.
[33] A. Chakraborty, R. Tangestani, R. Batmaz, W. Muhammad, P. Plamondon, A. Wessman, L. Yuan, É. Martin, In-process failure analysis of thin-wall structures made by laser powder bed fusion additive manufacturing, J. Mater. Sci. Technol. 98 (2022) 233–243.
[34] Z. Chen, L. Yuan, H. Zhu, D. Ding, H. Li, et al., A comprehensive review and future perspectives of simulation approaches in wire arc additive manufacturing (WAAM), Int. J. Extreme Manuf. 138 (2024) 101129.
[35] M. Bayat, W. Dong, J. Thorborg, A.C. To, J.H. Hattel, A review of multi-scale and multi-physics simulations of metal additive manufacturing processes with focus on modeling strategies, Addit. Manuf. 47 (2021) 102278.
[36] H.L. Wei, T. Mukherjee, W. Zhang, J.S. Zuback, G.L. Knapp, A. De, T. DebRoy, Mechanistic models for additive manufacturing of metallic components, Prog. Mater. Sci. 116 (2021) 100703.
[37] S. Cadiou, M. Courtois, M. Carin, W. Berckmans, et al., 3D heat transfer, fluid flow and electromagnetic model for cold metal transfer wire arc additive manufacturing (Cmt-Waam), Addit. Manuf. 36 (2020) 101541.
[38] M. Zhou, Y. Liu, Z. Lin, Topology optimization of thermal conductive support structures for laser additive manufacturing, Comput. Methods Appl. Mech. Eng. 353 (2019) 24–43.
[39] R. Ranjan, C. Ayas, M. Langelaar, F. van Keulen, Controlling local overheating in topology optimization for additive manufacturing, Struct. Multidiscip. Optim. 65 (6) (2022) 162.
[40] R. Ranjan, Z. Chen, C. Ayas, M. Langelaar, F. Van Keulen, Overheating control in additive manufacturing using a 3D topology optimization method and experimental validation, Addit. Manuf. 61 (2023) 103339.
[41] E. Mirkoohi, J. Ning, P. Bocchini, O. Fergani, K.-N. Chiang, S.Y. Liang, Thermal modeling of temperature distribution in metal additive manufacturing considering effects of build layers, latent heat, and temperature-sensitivity of material properties, J. Manuf. Mater. Process. 2 (3) (2018) 63.
[42] F.P. Incropera, D.P. DeWitt, Fundamentals of heat transfer (1981).
[43] H. Yeung, B. Lane, J. Fox, Part geometry and conduction-based laser power control for powder bed fusion additive manufacturing, Addit. Manuf. 30 (2019) 100844.
[44] J. Wu, N. Aage, R. Westermann, O. Sigmund, Infill optimization for additive manufacturing—approaching bone-like porous structures, IEEE Trans. Vis. Comput. Graph. 24 (2) (2017) 1127–1140.

[45] M. Chiumenti, E. Neiva, E. Salsi, M. Cervera, S. Badia, J. Moya, Z. Chen, C. Lee, C. Davies, Numerical modelling and experimental validation in selective laser melting, Addit. Manuf. 18 (2017) 171–185.
[46] P. Pichler, T. Leitner, E. Kaschnitz, J. Rattenberger, G. Pottlacher, Surface tension and thermal conductivity of NIST SRM 1155a (AISI 316L stainless steel), Int. J. Thermophys. 43 (5) (2022) 66.
[47] M. Watanabe, Y. Takahashi, S. Imaizumi, Y. Zhao, M. Adachi, M. Ohtsuka, A. Chiba, Y. Koizumi, H. Fukuyama, Thermophysical properties of liquid Co–Cr–Mo alloys measured by electromagnetic levitation in a static magnetic field, Thermochim. Acta 708 (2022) 179119.
[48] Y. Sun, H. Muta, K. Kurosaki, Y. Ohishi, Thermal and electrical conductivity of liquid Al–Si alloys, Int. J. Thermophys. 40 (3) (2019) 31.
[49] J.A. Van Toor, A knowledge based system to support design for selective laser melting, Ph.D. thesis, Delft University of Technology, 2014.
[50] S. Patel, J. Mekavibul, J. Park, A. Kolla, R. French, Z. Kersey, G.C. Lewin, Using machine learning to analyze image data from advanced manufacturing processes, in: 2019 Systems and Information Engineering Design Symposium (SIEDS), IEEE, 2019, pp. 1–5.
[51] I.A. Roberts, Investigation of residual stresses in the laser melting of metal powders in additive layer manufacturing (2012).
[52] W. Zhang, M. Tong, N.M. Harrison, Resolution, energy and time dependency on layer scaling in finite element modelling of laser beam powder bed fusion additive manufacturing, Addit. Manuf. 28 (2019) 610–620.
[53] A. Malmelöv, A. Lundbäck, L.-E. Lindgren, History reduction by lumping for time-efficient simulation of additive manufacturing, Metals 10 (1) (2019) 58.
[54] T.E. Bruns, D.A. Tortorelli, Topology optimization of non-linear elastic structures and compliant mechanisms, Comput. Methods Appl. Mech. Eng. 190 (26–27) (2001) 3443–3459.
[55] M.P. Bendsøe, O. Sigmund, Material interpolation schemes in topology optimization, Arch. Appl. Mech. 69 (1999) 635–654.
[56] C. Le, J. Norato, T. Bruns, C. Ha, D. Tortorelli, Stress-based topology optimization for continua, Struct. Multidiscip. Optim. 41 (2010) 605–620.
[57] F. Wang, B.S. Lazarov, O. Sigmund, On projection methods, convergence and robust formulations in topology optimization, Struct. Multidiscip. Optim. 43 (6) (2011) 767–784.
[58] B.S. Lazarov, F. Wang, O. Sigmund, Length scale and manufacturability in density-based topology optimization, Arch. Appl. Mech. 86 (2016) 189–218.
[59] K. Svanberg, The method of moving asymptotes—A new method for structural optimization, Int. J. Numer. Methods Eng. 24 (2) (1987) 359–373.
[60] O. Sigmund, Morphology-based black and white filters for topology optimization, Struct. Multidiscip. Optim. 33 (2007) 401–424.
[61] J. Pellens, G. Lombaert, B. Lazarov, M. Schevenels, Combined length scale and overhang angle control in minimum compliance topology optimization for additive manufacturing, Struct. Multidiscip. Optim. 59 (2019) 2005–2022.
[62] X. Qian, Undercut and overhang angle control in topology optimization: a density gradient based integral approach, Int. J. Numer. Methods Eng. 111 (3) (2017) 247–272.
[63] K. Liu, A. Tovar, An efficient 3D topology optimization code written in matlab, Struct. Multidiscip. Optim. 50 (2014) 1175–1196.